

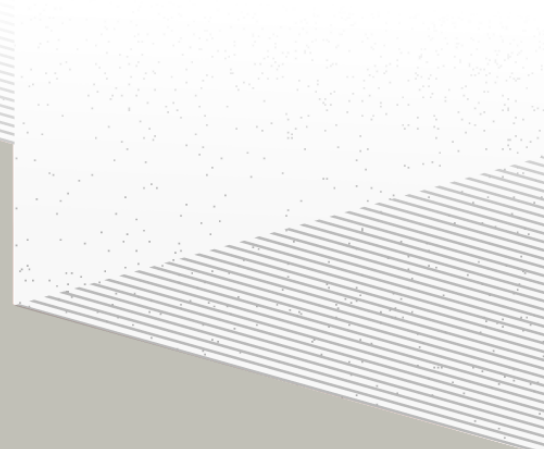
1

2

THÈSE DE DOCTORAT DE

L'UNIVERSITÉ DE NANTES

ÉCOLE DOCTORALE N°596
Matière, Molécules, Matériaux
Spécialité : *Physique des particules*



Par

Léonard Imbert

**Precision measurement of solar neutrino oscillation parameters
with the JUNO small PMTs system and test of the unitarity of the
PMNS matrix**

Thèse présentée et soutenue à Nantes, le Too soon and too early at the same time
Unité de recherche : Laboratoire SUBATECH, UMR 6457

Rapporteurs avant soutenance :

Someone	Very high position, Somewhere
Someone else	Another high position, Somewhere else

Composition du Jury :

Président :	Jacques Chirac	French president, France
Examinateurs :	Yoda	Master, Dagobha
Dir. de thèse :	Frédéric Yermia	Professeur, Université de Nantes
Co-dir. de thèse :	Benoit Viaud	Chargé de recherche, CNRS

Invité(s) :

Victor Lebrin Docteur, CNRS/SUBATECH

³ List of Abbreviations

ACU	Automatic Calibration Unit
BDT	Boosted Decision Tree
CD	Central Detector
CLS	Cable Loop System
CNN	Convolutional NN
DNN	Deep NN
GNN	Graph NN
GT	Guiding Tube
IBD	Inverse Beta Decay
IO	Inverse Ordering
JUNO	Jiangmen Underground Neutrino Observatory
LPMT	Large PMT
LS	Liquid Scintillator
MC	Monte Carlo simulation
ML	Machine Learning
NMO	Neutrino Mass Ordering
NN	Neural Network
NO	Normal Ordering
PE	Photo Electron
PMT	Photo-Multipliers Tubes
ROV	Remotely Operated under-LS Vehicle
SPMT	Small PMT
TR Area	Total Reflexion Area
TTS	Time Transit Spread
TT	Top Tracker
WCD	Water Cherenkov Detector

4 Contents

5	Contents	1
6	Remerciements	3
7	Introduction	5
8	1 Neutrino physics	7
9	1.1 Standard model	7
10	1.1.1 Limits of the standard model	7
11	1.2 Historic of the neutrino	7
12	1.3 Oscillation	7
13	1.3.1 Phenomologies	7
14	1.4 Open questions	7
15	2 The JUNO experiment	9
16	2.1 Neutrinos physics in JUNO	9
17	2.1.1 Reactor neutrino oscillation for NMO and precise measurements	10
18	2.1.2 Other physics	12
19	2.2 The JUNO detector	14
20	2.2.1 Principle of detection	14
21	2.2.2 Central Detector (CD)	15
22	2.2.3 Veto detector	18
23	2.3 Calibration strategy	18
24	2.3.1 Energy scale calibration	19
25	2.3.2 Calibration system	19
26	2.4 Software	20
27	2.5 State of the art of the Offline IBD reconstruction in JUNO	21
28	2.5.1 Interaction vertex reconstruction	22
29	2.5.2 Energy reconstruction	26
30	2.5.3 Machine learning for reconstruction	28
31	2.6 JUNO sensitivity to NMO and precise measurements	30
32	2.6.1 Fitting procedure	31
33	3 Machine learning and Artificial Neural Network	33
34	3.1 History of the Machine learning	33
35	3.2 Boosted Decision Tree (BDT)	33

36	3.3 Artificial Neural Network (NN)	33
37	3.3.1 Fully Connected Deep Neural Network (FCDNN)	33
38	3.3.2 Convolutional Neural Network (CNN)	33
39	3.3.3 Graph Neural Network (GNN)	33
40	3.3.4 Adversarial Neural Network (ANN)	33
41	4 Image recognition for IBD reconstruction with the SPMT system	35
42	5 Graph representation of JUNO for IBD reconstruction with the LPMT system	37
43	6 Reliability of machine learning methods	39
44	7 Discrimination of e+/e- events in JUNO	41
45	8 Conclusion	43
46	Bibliography	45

⁴⁷ **Remerciements**

48 Introduction

⁴⁹

Chapter 1

⁵⁰

Neutrino physics

⁵¹

The neutrino, or ν for the close friends, a fascinating and invisible particle. Some will say that dark matter also have those property but at least we are pretty confident that neutrinos exists.

⁵²

1.1 Standard model

⁵³

1.1.1 Limits of the standard model

⁵⁴

1.2 Historic of the neutrino

⁵⁵

First theories

⁵⁶

Discovery

⁵⁷

Milestones and anomalies

⁵⁸

1.3 Oscillation

⁵⁹

1.3.1 Phenomologies

⁶⁰

1.4 Open questions

Decrire le m
Regarder th
Kochebina
Limite du r
Interessant,
les neutrino
CP ? Pb des

⁶¹ **Chapter 2**

⁶² **The JUNO experiment**

⁶³ “Ave Juno, rosae rosam, et spiritus rex”. It means nothing but I found it in tone.

⁶⁴ The first idea of a medium baseline (~ 52 km) experiment, was explored in 2008 [1] where it was
⁶⁵ demonstrated that the Neutrino Mass Ordering (NMO) could be determined by a medium baseline
⁶⁶ experiment if $\sin^2(2\theta_{13}) > 0.005$ without the requirements of accurate knowledge of the reactor
⁶⁷ antineutrino spectra and the value of Δm_{32}^2 . From this idea is born the Jiangmen Underground
⁶⁸ Neutrino Observatory (JUNO) experiment.

⁶⁹ JUNO is a neutrino detection experiment under construction located in China. Its main objectives
⁷⁰ are the determination of the mass ordering at the $3\text{-}4\sigma$ level in 6 years of data taking and the mea-
⁷¹ surement at the sub-percent precision of the oscillation parameters Δm_{21}^2 , $\sin^2 \theta_{12}$, Δm_{32}^2 and with less
⁷² precision $\sin^2 \theta_{13}$ [2].



FIGURE 2.1 – On the left: Location of the JUNO experiment and its reactor sources in southern china. On the right: Aerial view of the experimental site

⁷³ For this JUNO will measure the electronic anti-neutrinos ($\bar{\nu}_e$) flux coming from the nuclear reac-
⁷⁴ tors of Taishan, Yangjiang, for a total power of 26.6 GW_{th} , and the Daya Bay power plant to a lesser
⁷⁵ extent. Details about the power plants and there expected flux of $\bar{\nu}_e$ can be found in the table 2.1. The
⁷⁶ distance of 53 km has been specifically chosen to maximize the disappearance probability of the $\bar{\nu}_e$.

⁷⁷ **2.1 Neutrinos physics in JUNO**

⁷⁸ Even if JUNO design (section 2.2) was optimized for the measurement of the NMO, its large
⁷⁹ detection volume, excellent energy resolution and background level and understanding make it also
⁸⁰ an excellent detector to measure the flux coming from other neutrino sources. Thus the scientific
⁸¹ program of JUNO extends way over reactor antineutrinos. The following section is an overview of
⁸² the different physics topic JUNO will contribute in the coming years.

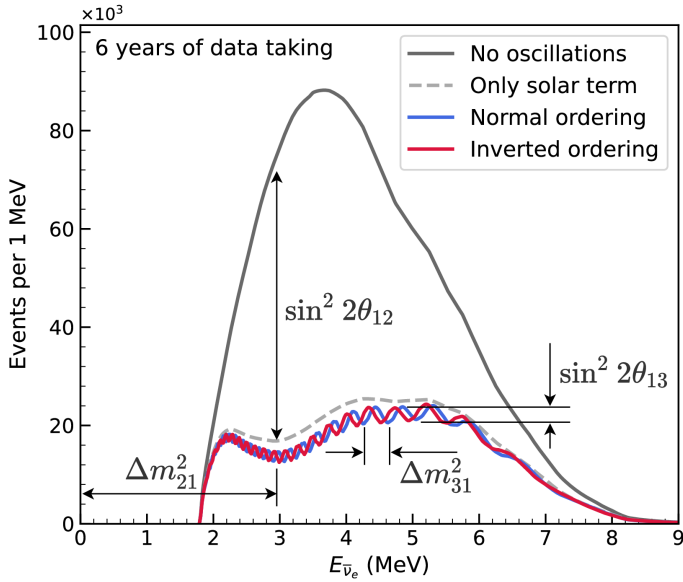


FIGURE 2.2 – Expected number of neutrinos event per MeV in JUNO after 6 years of data taking. The black curve shows the flux if there was no oscillation. The light gray curve shows the oscillation if only the solar terms are taken in account (θ_{12} , Δm_{21}^2). The blue and red curve shows the spectrum in the case of, respectively, NO and IO. The dependency of the oscillation to the different parameters are schematized by the double sided arrows. We can see the NMO sensitivity by looking at the fine phase shift between the red and the blue curve.

83 2.1.1 Reactor neutrino oscillation for NMO and precise measurements

Previous works [1, 3] shows that oscillation parameters and the NMO can be observed by looking at the $\bar{\nu}_e$ disappearance spectrum coming from medium baseline nuclear reactor. This disappearance probability can be expressed as [2] :

$$P(\bar{\nu}_e \rightarrow \bar{\nu}_e) = 1 - \sin^2 2\theta_{12} c_{13}^4 \sin^2 \frac{\Delta m_{21}^2 L}{4E} - \sin^2 2\theta_{13} \left[c_{12}^2 \sin^2 \frac{\Delta m_{31}^2 L}{4E} + s_{12}^2 \sin^2 \frac{\Delta m_{32}^2 L}{4E} \right]$$

84 Where $s_{ij} = \sin \theta_{ij}$, $c_{ij} = \cos \theta_{ij}$, E is the $\bar{\nu}_e$ energy and L is the baseline. We can see the sensitivity
 85 to the NMO in the dependency to Δm_{32}^2 and Δm_{31}^2 causing a phase shift of the spectrum as we can
 86 see in the figure 2.2. By carefully fitting this spectrum, one can extract the NMO and the oscillation
 87 parameters. The fit is reviewed in more details in the section 2.6.1. To reach the desired sensitivity,
 88 JUNO must meet multiple requirements but most notably:

- 89 1. An energy resolution of $3\%/\sqrt{E(\text{MeV})}$ to be able to distinguish the fine structure of the fast
 90 oscillation.
- 91 2. An energy precision of 1% in order to not err on the location of the oscillation pattern.
- 92 3. A baseline of 53 ± 0.5 km to maximise the $\bar{\nu}_e$ oscillation probability.
- 93 4. At least $\approx 100,000$ events to limit the spectrum distortion due to statistical uncertainties.

94 $\bar{\nu}_e$ flux coming from nuclear power plants

95 To get such high measurements precision, it is necessary to have a very good understanding of
 96 the sources characteristics. For its NMO and precise measurement studies, JUNO will observe the

97 energy spectrum of neutrinos coming from the nuclear power plants Taishan and Yangjiang's cores,
 98 located at 53 km of the detector to maximise the disappearance probability of the $\bar{\nu}_e$.

Reactor	Power (GW _{th})	Baseline (km)	IBD Rate (day ⁻¹)	Relative Flux (%)
Taishan	9.2	52.71	15.1	32.1
Core 1	4.6	52.77	7.5	16.0
Core 2	4.6	52.64	7.6	16.1
Yangjiang	17.4	52.46	29.0	61.5
Core 1	2.9	52.74	4.8	10.1
Core 2	2.9	52.82	4.7	10.1
Core 3	2.9	52.41	4.8	10.3
Core 4	2.9	52.49	4.8	10.2
Core 5	2.9	52.11	4.9	10.4
Core 6	2.9	52.19	4.9	10.4
Daya Bay	17.4	215	3.0	6.4

TABLE 2.1 – Characteristics of the nuclear power plants observed by JUNO. The IBD rate are estimated from the baselines, the reactors full thermal power, selection efficiency and the current knowledge of the oscillation parameters

99 The $\bar{\nu}_e$ coming from reactors are emitted from β -decay of unstable fission fragments. The Taishan
 100 and Yangjiang reactors are pressurised water reactor (PWR), the same type as Daya Bay. In those
 101 type of reactor more the 99.7 % and $\bar{\nu}_e$ are produced by the fissions of four fuel isotopes ²³⁵U, ²³⁸U,
 102 ²³⁹Pu and ²⁴¹Pu. The neutrino flux per fission of each isotope is determined by the inversion of the
 103 measured β spectra of fission product [4–8] or by calculation using the nuclear databases [9, 10]. The
 104 neutrino flux coming from a reactor at a time t can be predicted using

$$\phi(E_\nu, t)_r = \frac{W_{th}(t)}{\sum_i f_i(t) e_i} \sum_i f_i(t) S_i(E_\nu) \quad (2.1)$$

105 where $W_{th}(t)$ is the thermal power of the reactor, $f_i(t)$ is the fraction fission of the i th isotope, e_i its
 106 thermal energy released in each fission and $S_i(E_\nu)$ the neutrino flux per fission for this isotope. Using
 107 this method, the flux uncertainty is expected to be of an order of 2-3 % [11].

108 In addition to those prediction, a satellite experiment named TAO[12] will be setup near the
 109 reactor core Taishan-1 to measure with an energy resolution of 2% at 1 MeV the neutrino flux coming
 110 from the core. It will help identifying unknown fine structure and give more insight on the $\bar{\nu}_e$ flux
 111 coming from this reactor.

112 One the open issue about reactor anti-neutrinos flux is the so-called neutrino anomaly [13], an
 113 unexpected surplus of neutrino emission in the spectra around 5 MeV. Multiples scientists are trying
 114 to explain this surplus by advanced recalculation of the nuclei model during beta decay [14, 15] but
 115 no consensus on this issue has been reached yet.

116 Background in the neutrinos reactor spectrum

117 Considering the close reactor neutrinos flux as the main signal, the signals that are considered as
 118 background are:

- 119 — The geoneutrinos producing background in the 0.511 ~ 2.7 MeV region.
- 120 — The neutrinos coming from the other nuclear reactors around Earth.

121 In addition to all those physics signal, non-neutrinos signal that would mimic an IBD will also be
 122 present. It is composed of:

- 123 — The signal coming from radioactive decay (α , γ , β) from natural radioactive isotopes in the
 124 material of the detector.
- 125 — Cosmogenic event such as fast neutrons and activated isotopes induced by muons passing
 126 through the detector, most notably the spallation on ¹²C.

¹²⁷ All those events represent a non-negligable part of the spectrum as shown in figure 2.3.

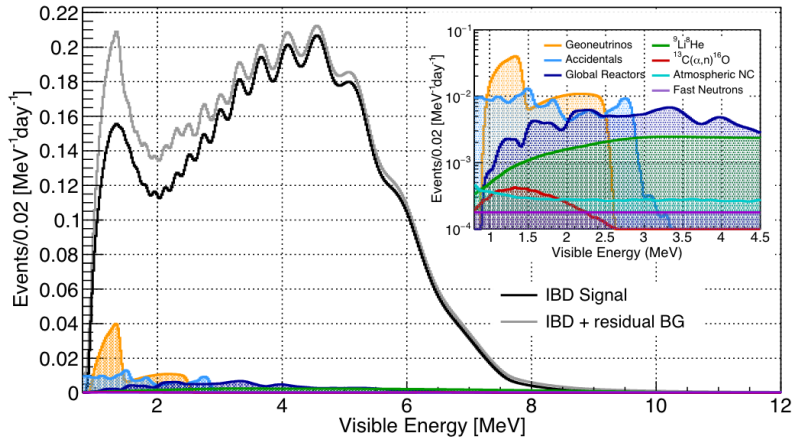


FIGURE 2.3 – Expected visible energy spectrum measured with the LPMT system with (grey) and without (black) backgrounds. The background amount for about 7% of the IBD candidate and are mostly localized below 3 MeV [11]

¹²⁸ Identification of the mass ordering

¹²⁹ To identify the mass ordering, we fit the neutrino energy spectrum under the two hypothesis of
¹³⁰ NO and IO. Those two fit give us two χ^2 , respectively χ^2_{NO} and χ^2_{IO} . By computing the difference
¹³¹ $\Delta\chi^2 = \chi^2_{NO} - \chi^2_{IO}$ we can determine the most probable mass ordering: NO if $\Delta\chi^2 > 0$ and IO
¹³² if $\Delta\chi^2 < 0$. Current studies shows that the expected sensitivity the mass ordering would be of
¹³³ 3.4σ after 6 years of data taking in nominal setup[2]. More detailed explanations about the fitting
¹³⁴ procedure can be found in the section 2.6.1.

¹³⁵ Precise measurement of the oscillations parameters

¹³⁶ The oscillations parameters θ_{12} , θ_{13} , Δm_{21}^2 , Δm_{31}^2 are free parameters in the fit of the oscillation
¹³⁷ spectrum. The precision on those parameters have been estimated and are shown in table 2.2. Wee
¹³⁸ see that for θ_{12} , Δm_{21}^2 , Δm_{31}^2 , precision at 6 years is better than the reference precision by an order of
¹³⁹ magnitude [11]

	Central Value	PDG 2020	100 days	6 years	20 years
$\Delta m_{31}^2 (\times 10^{-3} \text{ eV}^2)$	2.5283	± 0.034 (1.3%)	± 0.021 (0.8%)	± 0.0047 (0.2%)	± 0.0029 (0.1%)
$\Delta m_{21}^2 (\times 10^{-3} \text{ eV}^2)$	7.53	± 0.18 (2.4%)	± 0.074 (1.0%)	± 0.024 (0.3%)	± 0.017 (0.2%)
$\sin^2 \theta_{12}$	0.307	± 0.013 (4.2%)	± 0.0058 (1.9%)	± 0.0016 (0.5%)	± 0.0010 (0.3%)
$\sin^2 \theta_{13}$	0.0218	± 0.0007 (3.2%)	± 0.010 (47.9%)	± 0.0026 (12.1%)	± 0.0016 (7.3%)

TABLE 2.2 – A summary of precision levels fir the oscillation parameters. The reference value (PDG 2020 [16]) is compared with 100 days, 6 years and 20 years of JUNO data taking.

¹⁴⁰ 2.1.2 Other physics

¹⁴¹ While the design of JUNO is tailored to measure $\bar{\nu}_e$ coming from nuclear reactor, JUNO will be
¹⁴² able to detect neutrinos coming from other sources thus allowing for a wide range of physics studies
¹⁴³ as detailed in the table 2.3 and in the following sub-sections.

Research	Expected signal	Energy region	Major backgrounds
Reactor antineutrino	60 IBDs/day	0–12 MeV	Radioactivity, cosmic muon
Supernova burst	5000 IBDs at 10 kpc	0–80 MeV	Negligible
DSNB (w/o PSD)	2300 elastic scattering		
Solar neutrino	2–4 IBDs/year	10–40 MeV	Atmospheric ν
Atmospheric neutrino	hundreds per year for ${}^8\text{B}$	0–16 MeV	Radioactivity
Geoneutrino	hundreds per year	0.1–100 GeV	Negligible
	≈ 400 per year	0–3 MeV	Reactor ν

TABLE 2.3 – Detectable neutrino signal in JUNO and the expected signal rates and major background sources

¹⁴⁴ **Geoneutrinos**

¹⁴⁵ Geoneutrinos designate the antineutrinos coming from the decay of long-lived radioactive elements inside the Earth. The 1.8 MeV threshold necessary for the IBD makes it possible to measure ¹⁴⁶ geoneutrinos from ${}^{238}\text{U}$ and ${}^{232}\text{Th}$ decay chains. The studies of geoneutrinos can help refine the Earth ¹⁴⁷ crust models but is also necessary to characterise their signal, as they are a background to the mass ¹⁴⁸ ordering and oscillations parameters studies.

¹⁵⁰ **Atmospheric neutrinos**

¹⁵¹ Atmospheric neutrinos are neutrinos originating from the decay of π and K particles that are ¹⁵² produced in extensive air showers initiated by the interactions of cosmic rays with the Earth atmosphere. Earth is mostly transparent to neutrinos below the PeV energy, thus JUNO will be able to ¹⁵³ see neutrinos coming from all directions. Their baseline range is large (15km \sim 13000km), they can ¹⁵⁴ have energy between 0.1 GeV and 10 TeV and will contain all neutrino and antineutrinos flavour. ¹⁵⁵ Their studies is complementary to the reactor antineutrinos and can help refine the constraints on ¹⁵⁶ the NMO [2].

¹⁵⁸ **Supernovae burst neutrinos**

¹⁵⁹ Neutrinos are crucial component during all stages of stellar collapse and explosion. Detection ¹⁶⁰ of neutrinos coming for core collapse supernovae will provide us important informations on the ¹⁶¹ mechanisms at play in those events. Thanks to its 20 kt LS, JUNO has excellent capabilities to detect ¹⁶² all flavour of the $\mathcal{O}(10 \text{ MeV})$ postshock neutrinos, and using neutrinos of the $\mathcal{O}(1 \text{ MeV})$ will give ¹⁶³ informations about the pre-supernovae neutrinos. All those informations will allow to disentangle ¹⁶⁴ between the multiple hydro-dynamic models that are currently used to describe the different stage ¹⁶⁵ of core-collapse supernovae.

¹⁶⁶ **Diffuse supernovae neutrinos background**

¹⁶⁷ Core-collapse supernovae in our galaxy are rare events, but they frequently occur throughout the ¹⁶⁸ visible Universe sending burst of neutrinos in direction of the Earth. All those events contributes to ¹⁶⁹ a low background flux of low-energy neutrinos called the Diffuse Supernovae Neutrino Background ¹⁷⁰ (DSNB). Its flux and spectrum contains informations about the red-shift dependent supernovae rate, ¹⁷¹ the average supernovae neutrino energy and the fraction of black-hole formation in core-collapse ¹⁷² supernovae. Depending of the DSNB model, we can expect 2-4 IBD events per year in the energy range ¹⁷³ above the reactor $\bar{\nu}_e$ signal, which is competitive with the current Super-Kamiokande+Gadolinium ¹⁷⁴ phase [17].

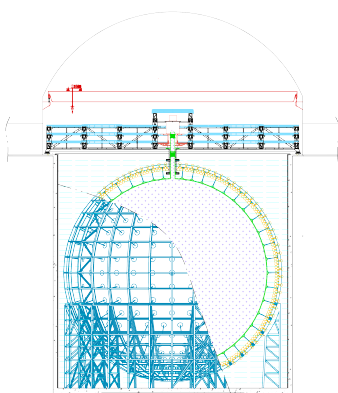
175 **Beyond standard model neutrinos interactions**

176 JUNO will also be able to probe for beyond standard model neutrinos interactions. After the
177 main physics topics have been accomplished, JUNO could be upgraded to probe for neutrinoless
178 beta decay ($0\nu\beta\beta$). The detection of such event would give critical informations about the nature
179 of neutrinos, is it a majorana or a dirac particle. JUNO will also be able to probe for neutrinos that
180 would come for the decay or annihilation of Dark Matter inside the sun and neutrinos from putative
181 primordial black hole. Through the unitary test of the mixing matrix, JUNO will be able to search
182 for light sterile neutrinos. Thanks to JUNO sensitivity, multiple other exotic can be performed on
183 neutrino related beyond standard model interactions.

184 **2.2 The JUNO detector**

185 The JUNO detector is a scintillator detector buried 693.35 meters under the ground (1800 meters
186 water equivalent). It consist of Central Detector (CD), a water pool and a Top Tracker (TT) as showed
187 in figure 2.4a The CD is an acrylic vessel containing the 20 ktons of LS. It is supported by a stainless
188 steel structure and is immersed in that water pool that is used as shielding from external radiation
189 and as a cherenkov detector for the background. The top of the experiment is partially covered by
190 the TT, a plastic scintillator detector which is use to detect the atmospheric muons background acting
191 as veto detector.

192 The top of the experiment also host the LS purification system, a water purification system, a
193 ventilation system to get rid of the potential radon in the air. The CD is observed by two system of
194 Photo-Multipliers Tubes (PMT). They are attached to the steel structure and their electronic readout
195 is submersed near them. A third system of PMT is also installed on the structure but are facing
196 outward of the CD, instrumenting the water to be cherenkov detector. The CD and the cherenkov
197 detector are optically separated by Tyvek sheet. A chimney for LS filling and purification and for
198 calibration operations connects the CD to the experimental hall from the top.



(A) Schematics view of the JUNO detector.



(B) Top down view of the JUNO detector under construction

199 This section cover in details the different components of the detector and the detection systems.

200 **2.2.1 Principle of detection**

The CD will detect the neutrino and measure their energy mainly via an Inverse Beta Decay (IBD) interaction with proton (mainly ^{12}C and H) in the LS:

$$\bar{\nu}_e + p \rightarrow n + e^+$$

Kinematics calculation shows that this interaction has an energy threshold for the $\bar{\nu}_e$ of $(m_n + m_e - m_p) \approx 1.806$ MeV [18] where m_λ is the mass of the λ particle. This threshold make the experiment blind to very low energy neutrinos. The residual energy $E_\nu - 1.806$ MeV is be distributed as kinetic energy between the positron and the neutron. The energy of the emitted positron E_e is given by [18]

$$E_e = \frac{(E_\nu - \delta)(1 + \epsilon_\nu) + \epsilon_\nu \cos \theta \sqrt{(E_\nu - \delta)^2 + \kappa m_e^2}}{\kappa} \quad (2.2)$$

where $\kappa = (1 + \epsilon_\nu)^2 - \epsilon_\nu^2 \cos^2 \theta \approx 1$, $\epsilon_\nu = \frac{E_\nu}{m_p} \ll 1$ and $\delta = \frac{m_n^2 - m_p^2 - m_e^2}{2m_p} \ll 1$. We can see from this equation that the positron energy is strongly correlated to the neutrino energy.

The positron and the neutron will then propagate in the detection medium, the Liquid Scintillator (LS), loosing their kinetic energy by exciting the molecule of the LS (more details in section 2.2.2). Once stopped, the positron will annihilate with an electron from the medium producing two 511 KeV gamma. Those gamma will themselves interact with the LS, exciting it before being absorbed by photoelectrical effect. The neutron will be captured by an hydrogen, emitting a 2.2 MeV gamma in the process. This gamma will also deposit its energy before being absorbed by the LS.

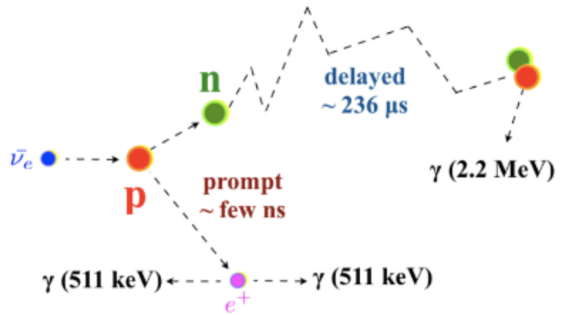


FIGURE 2.5 – Schematics of an IBD interaction in the central detector of JUNO

The scintillation photons have an UV frequency and will be captured by PMTs observing the CD. The analog signal of the PMTs digitized by the electronic is the signal of our experiment. The signal produced by the positron is subsequently called the prompt signal, and the signal coming from the neutron the delayed signal. This naming convention come from the fact that the positron will deposit its energy rather quickly (few ns) where the neutron will take a bit more time (~ 236 μ s).

2.2.2 Central Detector (CD)

The central detector, composed of 20 ktons of Liquid Scintillator (LS), is the main part of JUNO. The LS is contained in a spherical acrylic vessel supported by a stainless steel structure. The CD and its structural support are submerged in a cylindrical water pool of 43.5m diameter and 44m height. We're confident that the water pool provide sufficient buffer protection in every direction against the rock radioactivity.

Acrylic vessel

The acrylic vessel is a spherical vessel of inner diameter of 35.4 m and a thickness of 120 mm. It is assembled from 265 acrylic panels, thermo bonded together. The acrylic recipes has been carefully tuned with extensive R&D to ensure it does not include plasticizer and anti-UV material that would stop the scintillation photons. Those panels requires to be pure of radioactive materials to not cause background. Current setup where the acrylic panels are molded in cleanrooms of class 10000, let us reach a uranium and thorium contamination of <0.5 ppt. The molding and thermoforming processes is optimized to increase the assemblage transparency in water to >96%. The acrylic vessel

is supported by a stainless steel structure via supporting node (fig 2.6). The structure and the nodes are designed to be resilient to natural catastrophic events such as earthquake and can support many times the effective load of the acrylic vessel.

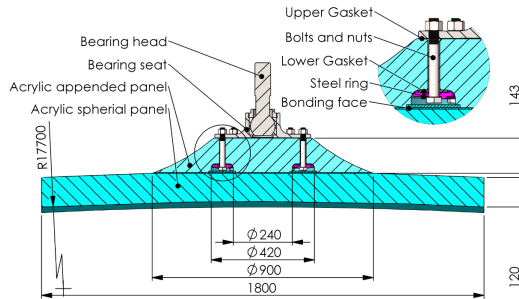


FIGURE 2.6 – Schematics of the supporting node for the acrylic vessel

235 Liquid scintillator

236 The Liquid Scintillator (LS) has a similar recipe as the one used in Daya Bay [19] but without
 237 gadolinium doping. It is made of three components, necessary to shift the wavelength of emitted
 238 photons to prevent their reabsorption:

- 239 1. The detection medium, the *linear alkylbenzene* (LAB). Selected because of its excellent trans-
 240 parency, high flash point, low chemical reactivity and good light yield. Accounting for \sim
 241 98% of the LS, it is the main component with which ionizing particles and gamma interact.
 242 Charged particles will collide with its electronic cloud transferring energy to the molecules,
 243 gamma will interact via compton effect with the electronic cloud before finally be absorbed
 244 via photoelectric effect.
- 245 2. The second component of the LS is the *2,5-diphenyloxazole* (PPO). A fraction of the excitation
 246 energy of the LAB is transferred to the PPO, mainly via non radiative process [20]. The
 247 PPO molecules de-excites in the same way, transferring their energy to the bis-MSB. The PPO
 248 makes for 1.5 % of the LS.
- 249 3. The last component is the *p-bis(o-methylstyryl)-benzene* (bis-MSB). Once excited by the PPO, it
 250 will emit photon with an average wavelength of \sim 430 nm (full spectrum in figure 2.7) that
 251 can be detected by our photo-multipliers systems. It amount for \sim 0.5% of the LS.

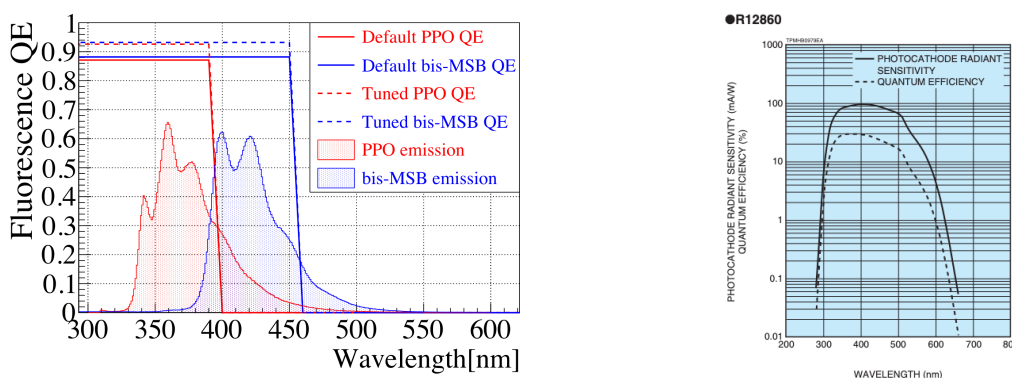


FIGURE 2.7 – On the left: Quantum efficiency (QE) and emission spectrum of the LAB and the bis-MSB [19]. On the right: Sensitivity of the Hamamatsu LPMT depending on the wavelength of the incident photons [21].

This formula has been optimized using dedicated studies with a Daya Bay detector [19, 22] to reach the requirements for the JUNO experiment:

- A light yield / MeV of the amount of 10^4 photons to maximize the statistic in the energy measurement.
- An attenuation length comparable to the size of the detector to prevent losing photons during their propagation in the LS. The final attenuation length is 25.8m [23] to compare with the CD diameter of 35.4m.
- Uranium/Thorium radiopurity to prevent background signal. The reactor neutrino program require a contamination fraction $F < 10^{-15}$ while the solar neutrino program require $F < 10^{-17}$.

The LS will frequently be purified and tested in the Online Scintillator Internal Radioactivity Investigation System (OSIRIS) [24] to ensure that the requirements are kept during the lifetime of the experiment.

Large Photo-Multipliers Tubes(LPMTs)

The scintillation light produced by the LS is then collected by Photo-Multipliers Tubes (PMT) that transform the incoming photon into an electric signal. As described in figure 2.8, the incident photons interact with the photocathode via photoelectric effect producing an electron called a Photo-Electron (PE). This PE is then focused on the dynodes where the high voltage will allow it to be multiplied. After multiple amplification the resulting charge - in coulomb [C] - is collected by the anode and the resulting electric signal can be digitalized by the readout electronics from which the charge and timing can be extracted.

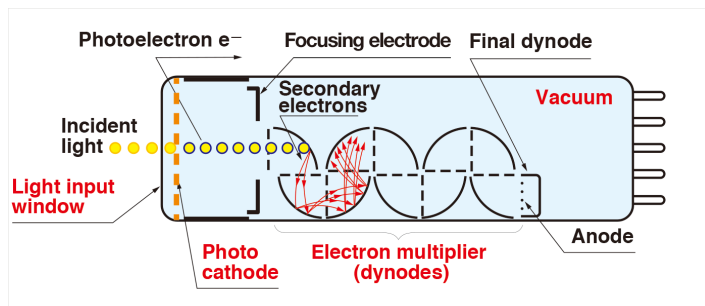


FIGURE 2.8 – Schematic of a PMT

The Large Photo-Multipliers Tubes (LPMT), used in the central detector and in the water pool, are 20-inch (50.8 cm) radius PMTs. ~ 5000 dynode-PMTs [21] were produced by the Hamamatsu[®] company and ~ 15000 Micro-Channel Plate (MCP) [25] by the NNVT[®] company. This system is the one responsible for the energy measurement with a energy resolution of $3\%/\sqrt{E}$, resolution necessary for the mass ordering measurement. To reach this precision, the system is composed of 17612 PMTs quasi uniformly distributed over the detector for a coverage of 75.2% reaching ~ 1800 PE/MeV or $\sim 2.3\%$ resolution due to statistic, leaving $\sim 0.7\%$ for the systematic uncertainties. To maintain the resolution over the lifetime of the experiment, JUNO require a failure rate $< 1\%$ over 6 years.

The LPMTs electronic are divided in two parts. One "near", located underwater, in proximity of the LPMT to reduce the cable length between the PMT and early electronic. A second one, outside of the detector that is responsible for higher level analysis before sending the data to the DAQ.

The light yield per MeV induce that a LPMT can collect between 1 and 1000 PE per event, causing non linearity in the PMT response that need to be understood and calibrated, see section 2.3 for more details.

288 **Small Photo-Multipliers Tubes (SPMTs)**

289 The Small PMT (SPMTs) system is made of 3-inch (7.62 cm) PMTs. They will be used in the CD
 290 as a secondary detection system. Those 25600 SPMTs will observe the same events as the LPMTs,
 291 thus sharing the physics and detector systematics up until the photon conversion. With a detector
 292 coverage of 2.7%, this system will collect ~ 43 PE/MeV for a final energy resolution of $\sim 17\%$.
 293 This resolution is not enough to measure the NMO, θ_{13} , Δm_{31}^2 but will be sufficient to independently
 294 measure θ_{12} and Δm_{21}^2 .

295 Due to the low PE rate, SPMTs will be running in photo-counting mode in the reactor range thus
 296 will be insensitive to non-linearity effect. Also, due to their smaller size and electronics, SPMTs have
 297 a better timing resolutions than the LPMTs. At higher energy range, like supernovae events, LPMTs
 298 will saturate where SPMTs due to their lower PE collection will to produce a reliable measure of the
 299 energy spectrum.

300 The Data Acquisition System (DAQ) is designed to support the event rate of IBD, background,
 301 dark noise and supplementary storage buffers are present in the LPMT electronics to withstand the
 302 event rate during supernovae burst.

303 **2.2.3 Veto detector**

304 The CD will be bathed in constant background noise coming from numerous sources : the ra-
 305 dioactivity from surrounding rock and its own components or from the flux of cosmic muons. This
 306 background needs to be rejected to ensure the purity of the IBD spectrum. To prevent a big part of
 307 them, JUNO use two veto detector that will tag events as background before CD analysis.

308 **Cherenkov in water pool**

309 The Water Cherenkov Detector (WCD) is the instrumentalization of the water buffer around the
 310 CD. When high speed charged particles will pass through the water, they will produced cherenkov
 311 photons. The light will be collected by 2400 MCP LPMTs installed on the outer surface of the CD
 312 structure. The muons veto strategy is based on a PMT multiplicity condition. WCD PMTs are
 313 grouped in ten zones: 5 in the top, 5 in the bottom. A veto is raised either when more than 19
 314 PMTs are triggered in one zone or when two adjacent zones simultaneously trigger more than 13
 315 PMTs. Using this trigger, we expect to reach a muon detection efficiency of 99.5% while keeping the
 316 noise at reasonable level.

317 **Top tracker**

318 The JUNO Top Tracker (TT) is a plastic scintillator detector located on the top of the experiment
 319 (see figure 2.9). Made from plastic scintillator from OPERA [26] layered horizontally in 3 layers on
 320 the top of the detector, the TT will be able to detect incoming atmospheric muons. With its coverage,
 321 about 1/3 of the of all atmospheric muons that passing through the CD will also pass through the 3
 322 layer of the detector. While it does not cover the majority of the CD, the TT is particularly effective
 323 to detect muons coming through the filling chimney region which might present difficulties from the
 324 other subsystems in some classes of events.

325 **2.3 Calibration strategy**

326 The calibration is a crucial part of the JUNO experiment. Because we are looking at civil reactor
 327 neutrino it might be impossible to run measurement without signal, it would need to shut down
 328 every reactor from the Taishan and Yangjiang power plants which is realistically impossible. Because
 329 of this continuous rate, low frequency signal event, we need high frequency, recognisable sources in
 330 the energy range of interest : [0-12] MeV for the positron signal and 2.2 MeV for the neutron capture.
 331 It is expected that the CD response will be different depending on the type of particle, due to the

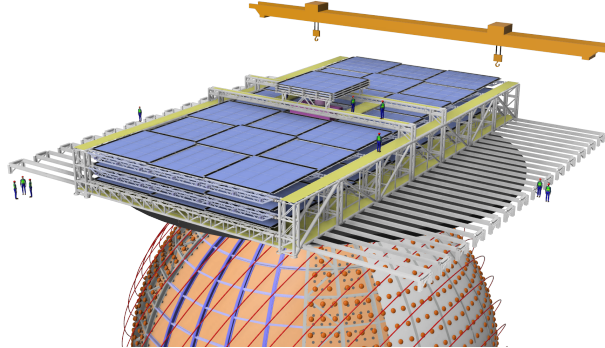


FIGURE 2.9 – The JUNO top tracker

interaction with LS, the position on the event and the optical response of the acrylic sphere (see section 2.5). We also expect a non-linear energy response of the CD due to the LS properties [19] but also due to the saturation of the LPMTs system when collecting a large amount of PE [27].

2.3.1 Energy scale calibration

While electrons and positrons sources would be ideal, for a large LS detector thin-walled electrons or positrons sources could lead to leakage of radionuclides causing radioactive contamination. Instead, we consider gamma sources in the range of the prompt energy of IBDs. The sources are reported in table 2.4.

Sources / Processes	Type	Radiation
^{137}Cs	γ	0.0662 MeV
^{54}Mn	γ	0.835 MeV
^{60}Co	γ	1.173 + 1.333 MeV
^{40}K	γ	1.461 MeV
^{68}Ge	e^+	annihilation 0.511 + 0.511 MeV
$^{241}\text{Am-Be}$	n, γ	neutron + 4.43 MeV (12C*)
$^{241}\text{Am-}^{13}\text{C}$	n, γ	neutron + 6.13 MeV (16O*)
$(n, \gamma)p$	γ	2.22 MeV
$(n, \gamma)^{12}\text{C}$	γ	4.94 MeV or 3.68 + 1.26 MeV

TABLE 2.4 – List of sources and their process considered for the energy scale calibration

For the ^{68}Ge source, it will decay in ^{68}Ga via electron capture, which will itself β^+ decay into ^{68}Zn . The positrons will be absorbed by the enclosure so only the annihilation gamma will be released. In addition, (α, n) sources like $^{241}\text{Am-Be}$ and $^{241}\text{Am-}^{13}\text{C}$ are used to provide both high energy gamma and neutrons, which will later be captured in the LS producing the 2.2 MeV gamma.

From this calibration we call E_{vis} the "visible energy" that is reconstructed by our current algorithms and we compare it to the true energy deposited by the calibration source. The results shown in figure 2.10 show the expected response of the detector from calibration sources. The non-linearity is clearly visible from the E_{vis}/E_{true} shape. See [28] for more details.

2.3.2 Calibration system

The non-uniformity due to the event position in the detector (more details in section 2.5) will be studied using multiple systems that are schematized in figure 2.11. They allow to position sources at different location in the CD.

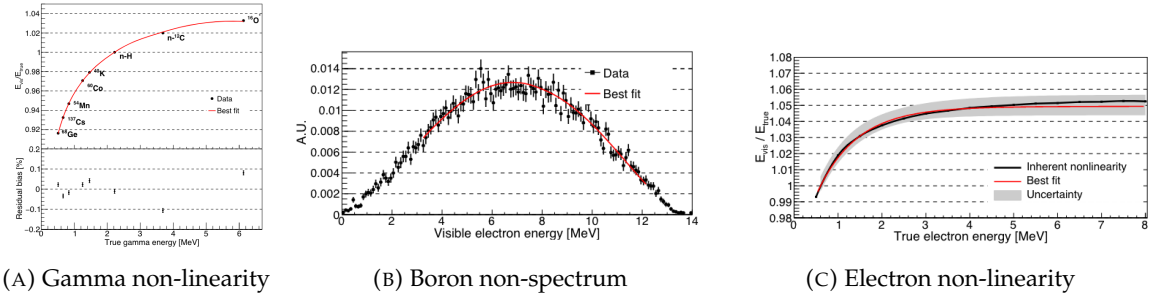


FIGURE 2.10 – Fitted and simulated non linearity of gamma, electron sources and from the ^{12}B spectrum. Black points are simulated data. Red curves are the best fits

- For a one-dimension vertical calibration, the Automatic Calibration Unit (ACU) will be able to deploy multiple radioactive sources or a pulse laser diffuser ball along the central axis of the CD through the top chimney. The source position precision is less than 1cm.
- For off-axis calibration, a calibration source attached to a Cable Loop System (CLS) can be moved on a vertical half-plane by adjusting the length of two connection cable. Two set of CSL will be deployed to provide a 79% effective coverage of a vertical plane.
- A Guiding Tube (GT) will surround the CD to calibrate the non-uniformity of the response at the edge of the detector
- A Remotely Operated under-LS Vehicle (ROV) can be deployed to desired location inside LS for a more precise and comprehensive calibration. The ROV will also be equipped with a camera for inspection of the CD.

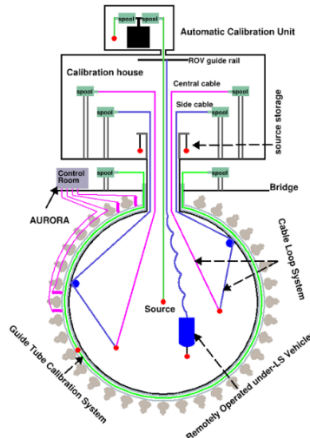


FIGURE 2.11 – Overview of the calibration system

- 363 The preliminary calibration program is depicted in table 2.5.

364 2.4 Software

365 The simulation, reconstruction and analysis algorithms are all packaged in the JUNO software,
 366 subsequently called the software. It is composed of multiple components integrated in the SNiPER
 367 [29] framework:

- 368 — Various primary particles simulators for the different kind of events, background and calibra-
 369 tion sources.

Program	Purpose	System	Duration [min]
Weekly calibration	Neutron (Am-C)	ACU	63
	Laser	ACU	78
Monthly calibration	Neutron (Am-C)	ACU	120
	Laser	ACU	147
	Neutron (Am-C)	CLS	333
	Neutron (Am-C)	GT	73
Comprehensive calibration	Neutron (Am-C)	ACU, CLS and GT	1942
	Neutron (Am-Be)	ACU	75
	Laser	ACU	391
	^{68}Ge	ACU	75
	^{137}Cs	ACU	75
	^{54}Mn	ACU	75
	^{60}Co	ACU	75
	^{40}K	ACU	158

TABLE 2.5 – Calibration program of the JUNO experiment

- A Geant4 [30–32] Monte Carlo (MC) simulation containing the detectors geometries, a custom optical model for the LS and the supporting structures of the detectors. The Geant4 simulation integrate all relevant physics process for JUNO, validated by the collaboration. This step of the simulation is commonly called *Detsim* and compute up to the production of photo-electrons in the PMTs. The optics properties of the different materials and detector components have been measured beforehand to be used to define the material and surfaces in the simulation.
 - An electronic simulation, simulating the response waveform of the PMTs, tracking it through the digitization process, accounting for effects such as non-linearity, dark noise, Time Transit Spread (TTS), pre-pulsing, after-pulsing and ringing if the waveform. It's also the step handling the event triggers and mixing. This step is commonly referenced as *Elecsim*.
 - A waveform reconstruction where the digitized waveform are filtered to remove high-frequency white noise and then deconvoluted to yield time and charge informations of the photons hits on the PMTs. This step is commonly referenced as *Calib*.
 - The charge and time informations are used by reconstruction algorithms to reconstruct the interaction vertex and the deposited energy. This step is commonly reported as *Reco*. See section 2.5 for more details on the reconstruction.
 - Once the singular events are reconstructed, they go through event pairing and classification to select IBD events. This step is named Event Classification.
 - The purified signal is then analysed by the analysis framework which depend of the physics topic of interest.
- The steps Reco and Event Classification are divided into two category of algorithm. Fast but less accurate algorithms that are running during the data taking designated as the *Online* algorithms. Those algorithm are used to take the decision to save the event on tape or to throw it away. More accurate algorithms that run on batch of events designated *Offline* algorithms. They are used for the physics analysis. The Offline Reco will be one of the main topic of interest for this thesis.

2.5 State of the art of the Offline IBD reconstruction in JUNO

The main reconstruction method currently run in JUNO is a data-driven method based on a likelihood maximization [33, 34] using only the LPMTs. The first step is to reconstruct the interaction vertex from which the energy reconstruction is dependent. It is also necessary for event pairing and classification.

400 **2.5.1 Interaction vertex reconstruction**

401 To start the likelihood maximization, a rough estimation of the vertex and of the event timing is
 402 needed. We start by estimating the vertex position using a charge based algorithm.

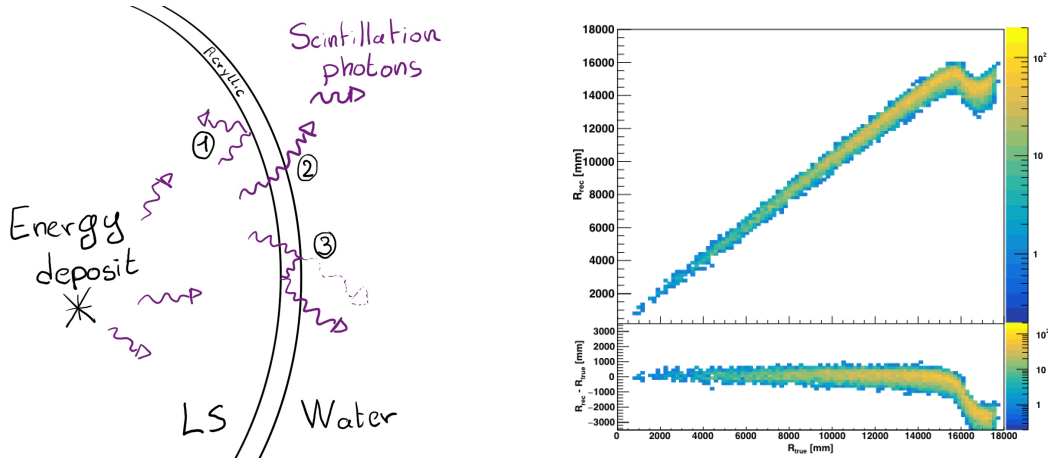
403 **Charge based algorithm**

404 The charge-based algorithm is basically base on the charge-weighted average of the PMT position.

$$\vec{r}_{cb} = a \cdot \frac{\sum_i q_i \cdot \vec{r}_i}{\sum_i q_i} \quad (2.3)$$

405 Where q_i is the reconstructed charge of the pulse of the i th PMT and \vec{r}_i is its position. \vec{r}_0 is the
 406 reconstructed interaction position. a is a scale factor introduced because a weighted average over
 407 a 3D sphere is inherently biased. Using calibration we can estimate $a \approx 1.3$ [35]. The results in
 408 figure 2.12b shows that the reconstruction is biased from around 15m and further. This is due to the
 409 phenomena called “total reflection area” or TR Area.

410 As depicted in the figure 2.12a the optical photons, given that they have a sufficiently large
 411 incidence angle, can be deviated of their trajectories when passing through the interfaces LS-acrylic
 412 and water-acrylic due to the optical index difference. This cause photons to be lost or to be detected
 413 by PMT further than anticipated if we consider their rectilinear trajectories. This cause the charge
 414 barycenter the be located closer to the center than the event really is.



(A) Illustration of the different optical photons reflection scenarios. 1 is the reflection of the photon at the interface LS-acrylic or acrylic-water. 2 is the transmission of the photons through the interfaces. 3 is the conduction of the photon in the acrylic.

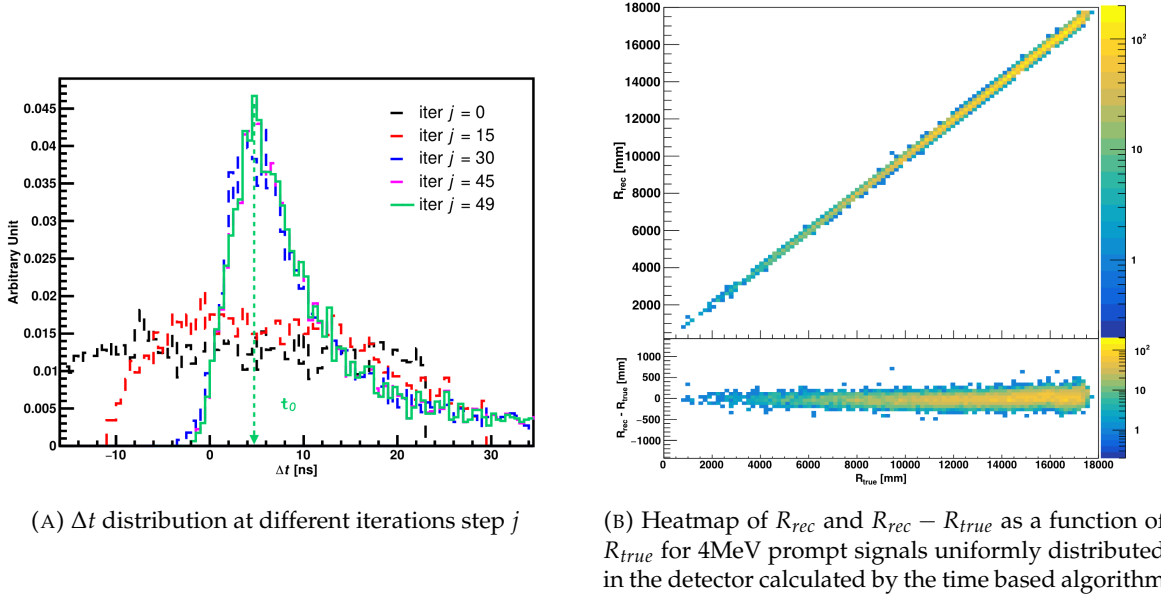
(B) Heatmap of R_{rec} and $R_{rec} - R_{true}$ as a function of R_{true} for 4MeV prompt signals uniformly distributed in the detector calculated by the charge based algorithm

FIGURE 2.12

415 It is to be noted that charge based algorithm, in addition to be biased near the edge of the detector,
 416 does not provide any information about the timing of the event. Therefore, a time based algorithm
 417 needs to be introduced to provide initial values.

418 **Time based algorithm**

419 The time based algorithm use the distribution of the time of flight corrections Δt (Eq 2.4) of an
 420 event to reconstruct its vertex and t_0 . It follow the following iterations:

(A) Δt distribution at different iterations step j (B) Heatmap of R_{rec} and $R_{rec} - R_{true}$ as a function of R_{true} for 4MeV prompt signals uniformly distributed in the detector calculated by the time based algorithm

- 421 1. Use the charge based algorithm to get an initial vertex to start the iteration.
 422 2. Calculate the time of flight correction for the i th PMT using

$$\Delta t_i(j) = t_i - \text{tof}_i(j) \quad (2.4)$$

423 where j is the iteration step, t_i is the timing of the i th PMT, and tof_i is the time-of-flight of the
 424 photon considering an rectilinear trajectory and an effective velocity in the LS and water (see
 425 [35] for detailed description of this effective velocity). Plot the Δt distribution and label the
 426 peak position as Δt^{peak} (see fig 2.13a).

- 427 3. Calculate a correction vector $\vec{\delta}[\vec{r}(j)]$ as

$$\vec{\delta}[\vec{r}(j)] = \frac{\sum_i \left(\frac{\Delta t(j) - \Delta t^{\text{peak}}(j)}{\text{tof}_i(j)} \right) \cdot (\vec{r}_0(j) - \vec{r}_i)}{N^{\text{peak}}(j)} \quad (2.5)$$

428 where \vec{r}_0 is the vertex position at the beginning of this iteration, \vec{r}_i is the position of the i th
 429 PMT. To minimize the effect of scattering, dark noise and reflection, only the pulse happening
 430 in a time window (-10 ns, +5 ns) around Δt^{peak} are considered. N^{peak} is the number of PE
 431 collected in this time-window.

- 432 4. if $\vec{\delta}[\vec{r}(j)] < 1\text{mm}$ or $j \geq 100$, stop the iteration. Otherwise $\vec{r}_0(j+1) = \vec{r}_0(j) + \vec{\delta}[\vec{r}(j)]$ and go to
 433 step 2.

434 However because the earliest arrival time is used, t_i is related to the number photoelectrons N_i^{pe}
 435 detected by the PMT [36–38]. To reduce bias in the vertex reconstruction, the following equation is
 436 used to correct t_i into t'_i :

$$t'_i = t_i - p_0 / \sqrt{N_i^{\text{pe}}} - p_1 - p_2 / N_i^{\text{pe}} \quad (2.6)$$

437 The parameters (p_0, p_1, p_2) were optimized to (9.42, 0.74, -4.60) for Hamamatsu PMTs and (41.31,
 438 -12.04, -20.02) for NNVT PMTs [35]. The results presented in figure 2.13b shows that the time based
 439 algorithm provide a more accurate vertex and is unbiased even in the TR area. This results (\vec{r}_0, t_0) is
 440 used as initial value for the likelihood algorithm.

441 **Time likelihood algorithm**

442 The time likelihood algorithm use the residual time expressed as follow

$$t_{\text{res}}^i(\vec{r}_0, t_0) = t_i - \text{tof}_i - t_0 \quad (2.7)$$

443 In a first order approximation, the scintillator time response Probability Density Function (PDF)
 444 can be described as the emission time profile of the scintillation photons, the Time Transit Spread
 445 (TTS) and the dark noise of the PMTs. The emission time profile $f(t_{\text{res}})$ is described like

$$f(t_{\text{res}}) = \sum_k \frac{\rho_k}{\tau_k} e^{-\frac{t_{\text{res}}}{\tau_k}}, \sum_k \rho_k = 1 \quad (2.8)$$

446 as the sum of the k component that emit light in the LS each one characterised by it's decay time τ_k
 447 and intensity fraction ρ_k . The TTS component is expressed as a gaussian convolution

$$g(t_{\text{res}}) = \frac{1}{\sqrt{2\pi}\sigma} e^{-\frac{(t_{\text{res}}-\nu)^2}{2\sigma^2}} \cdot f(t_{\text{res}}) \quad (2.9)$$

448 where σ is the TTS of PMTs and ν is the average transit time. The dark noise is not correlated with any
 449 physical events and considered as constant rate over the time window considered T . By normalizing
 450 the dark noise probability $\epsilon(t_{\text{res}})$ as $\int_T \epsilon(t_{\text{res}}) dt_{\text{res}} = \epsilon_{\text{dn}}$, it can be integrated in the PDF as

$$p(t_{\text{res}}) = (1 - \epsilon_{\text{dn}}) \cdot g(t_{\text{res}}) + \epsilon(t_{\text{res}}) \quad (2.10)$$

451 The distribution of the residual time t_{res} of an event can then be compared to $p(t_{\text{res}})$ and the best
 452 vertex \vec{r}_0 and t_0 can be chosen by minimizing

$$\mathcal{L}(\vec{r}_0, t_0) = -\ln \left(\prod_i p(t_{\text{res}}^i) \right) \quad (2.11)$$

453 The parameter of Eq. 2.10 can be measured experimentally. The results shown in figure 2.14
 454 used PDF from monte carlo simulation. The results shows that $R_{\text{rec}} - R_{\text{true}}$ is biased depending
 455 on the energy. While this could be corrected using calibration, another algorithm based on charge
 456 likelihood was developed to correct this problem.

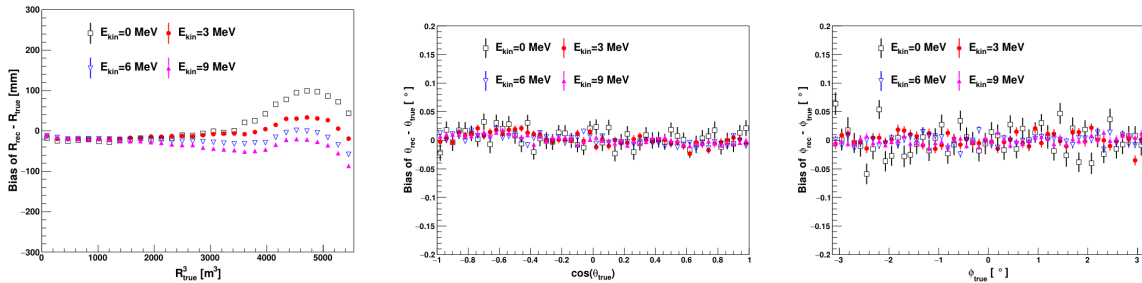


FIGURE 2.14 – Bias of the reconstructed radius R (left), θ (middle) and ϕ (right) for multiple energies by the time likelihood algorithm

457 **Charge likelihood algorithm**

458 Similarly to the time likelihood algorithms that use a timing PDF, the charge likelihood algorithm
 459 use a PE PDF for each PMT depending on the energy and position of the event. With $\mu(\vec{r}_0, E)$ the

mean expected number of PE detected by each PMT, the probability to observe N_{pe} in a PMT follow a Poisson distribution. Thus

— The probability to observe no hit ($N_{pe} = 0$) in the j th PMT is $P_{nohit}^j(\vec{r}_0, E) = e^{-\mu_j}$

— The probability to observe $N_{pe} \neq 0$ in the i th PMT is $P_{hit}^i(\vec{r}_0, E) = \frac{\mu^{N_{pe}} e^{-\mu_i}}{N_{pe}^i!}$

Therefore, the probability to observe a specific hit pattern can be expressed as

$$P(\vec{r}_0, E) = \prod_j P_{nohit}^j(\vec{r}_0, E) \cdot \prod_i P_{hit}^i(\vec{r}_0, E) \quad (2.12)$$

The best fit values of \vec{R}_0 and E can then be calculated by minimizing the negative log-likelihood

$$\mathcal{L}(\vec{r}_0, E) = -\ln(P(\vec{r}_0, E)) \quad (2.13)$$

In principle, $\mu_i(\vec{r}_0, E)$ could be expressed

$$\mu_i(\vec{r}_0, E) = Y \cdot \frac{\Omega(\vec{r}_0, r_i)}{4\pi} \cdot \epsilon_i \cdot f(\theta_i) \cdot e^{-\sum_m \frac{d_m}{\zeta_m}} \cdot E + \delta_i \quad (2.14)$$

where Y is the energy scale factor, $\Omega(\vec{r}_0, r_i)$ is the solid angle of the i th PMT, ϵ_i is its detection efficiency, $f(\theta_i)$ its angular response, ζ_m is the attenuation length in the materials and δ_i the expected number of dark noise.

However Eq. 2.14 assume that the scintillation light yield is linear with energy and describe poorly the contribution of indirect light, shadow effect due to the supporting structure and the total reflection effects. The solution is to use data driven methods to produce the pdf by using the calibrations sources and position described in section 2.3. In the results presented in figures 2.15, the PDF was produced using MC simulation and 29 specific calibrations position [35] along the Z-axis of the detector. We see that the charge likelihood algorithm show little bias in the TR area and a

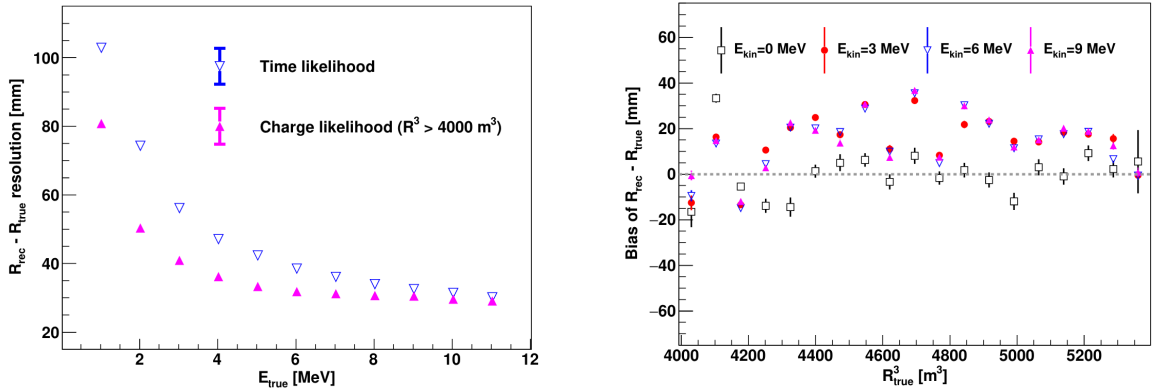


FIGURE 2.15 – On the left: Resolution of the reconstructed R as a function of the energy in the TR area ($R^3 > 4000 \text{ m}^3 \equiv R > 16 \text{ m}$) by the charge and time likelihood algorithms. On the right: Bias of the reconstructed R in the TR area for different energies by the charge likelihood algorithm

better resolution than the time likelihood. The figure 2.16 shows the radial resolution of the different algorithm presented for this section, we can see the refinement at each step and that the charge likelihood yield the best results.

The charge based likelihood algorithms already give use some information on the energy as Eq. 2.13 is minimized but the energy can be further refined as shown in the next section.

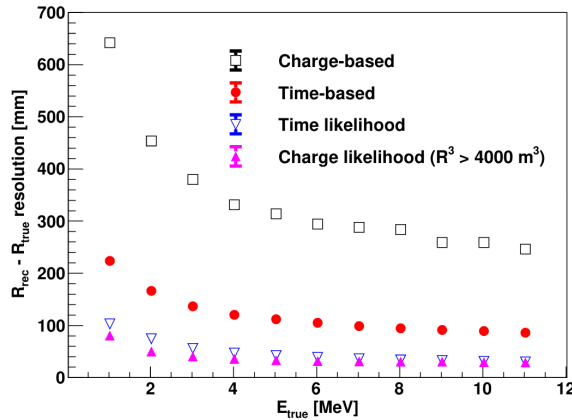


FIGURE 2.16 – Radial resolution of the different vertex reconstruction algorithms as a function of the energy

481 2.5.2 Energy reconstruction

482 As explained in section 2.1.1, energy resolution is crucial for the NMO and oscillation parameters
 483 measurements. Thus the energy reconstruction algorithm should take into consideration as much
 484 detector effect as possible. The following method is a data driven method based on calibration
 485 samples inspired by the charge likelihood algorithm described above [39].

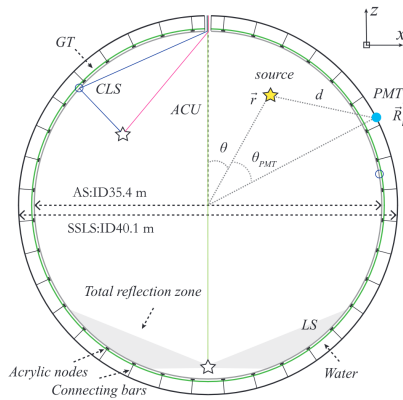


FIGURE 2.17 – Definition of the variables used in the energy reconstruction

486 Charge estimation

487 The most important element in the energy reconstruction is $\mu_i(\vec{r}_0, E)$ described in Eq. 2.14. For
 488 realistic cases, we also need to take into account the electronics effect that were omitted in the
 489 previous section. Those effect will cause a charge smearing due to the uncertainties in the N_{pe}
 490 reconstruction. Thus we define $\hat{\mu}^L(\vec{r}_0, E)$ which is the expected N_{pe}/E in the whole detector for an
 491 event with visible energy E_{vis} and position \vec{r}_0 . The position of the event and PMTs are now defined

⁴⁹² using $(r, \theta, \theta_{pmt})$ as defined in figure 2.17.

$$\hat{\mu}(r, \theta, \theta_{pmt}, E_{vis}) = \frac{1}{E_{vis}} \frac{1}{M} \sum_i^M \frac{\bar{q}_i - \mu_i^D}{\text{DE}_i}, \mu_i^D = \text{DNR}_i \cdot L \quad (2.15)$$

⁴⁹³ where i runs over the PMTs with the same θ_{pmt} , DE_i is the detection efficiency of the i th PMT. μ_i^D
⁴⁹⁴ is the expected number of dark noise photoelectrons in the time window L . The time window have
⁴⁹⁵ been optimized to $L = 280$ ns [39]. \bar{q}_i is the average recorded photoelectrons in the time window
⁴⁹⁶ and \hat{Q}_i is the expected average charge for 1 photoelectron. The N_{pe} map is constructed following the
⁴⁹⁷ procedure described in [34].

⁴⁹⁸ Time estimation

⁴⁹⁹ The second important observable is the hit time of photons that was previously defined in Eq.
⁵⁰⁰ 2.7. It is here refined as

$$t_r = t_h - \text{tof} - t_0 = t_{LS} + t_{TT} \quad (2.16)$$

⁵⁰¹ where t_h is the time of hit, t_{LS} is the scintillation time and t_{TT} the transit time of PMTs that is described
⁵⁰² by a gaussian

$$t_{TT} = \mathcal{N}(\bar{\mu}_{TT} + t_d, \sigma_{TT}) \quad (2.17)$$

⁵⁰³ where μ_{TT} is the mean transit time in PMTs, σ_{TT} is the Transit Time Spread (TTS) of the PMTs and t_d
⁵⁰⁴ is the delay time in the electronics. The effective refraction index of the LS is also corrected to take
⁵⁰⁵ into account the propagation distance in the detector.

⁵⁰⁶ The timing PDF $P_T(t_r | r, d, \mu_l, \mu_d, k)$ can now be generated using calibration sources [39]. This PDF
⁵⁰⁷ describe the probability that the residual time of the first photon hit is in $[t_r, t_r + \delta]$ with r the radius
⁵⁰⁸ of the event vertex, $d = |\vec{r} - \vec{r}_{PMT}|$ the propagation distance, μ_l and μ_d the expected number of PE
⁵⁰⁹ and dark noise in the electronic reading window and k is the detected number of PE.

⁵¹⁰ Now let denote $f(t, r, d)$ the probability density function of "photoelectron hit a time t" for an
⁵¹¹ event happening at r where the photons traveled the distance d in the LS

$$F(t, r, d) = \int_t^L f(t', r, d) dt' \quad (2.18)$$

⁵¹² Based on the PDF for one photon $k = 1$, one can define

$$P_T^l(t | k = n) = I_n^l [f_l(t) F_l^{n-1}(t)] \quad (2.19)$$

⁵¹³ where the indicator l means that the photons comes from the LS and I_n^l a normalisation factor. To this
⁵¹⁴ pdf we add the probability to have photons coming from the dark noise indicated by the indicator d
⁵¹⁵ using

$$f_d(t) = 1/L, F_d(t) = 1 - \frac{t}{L} \quad (2.20)$$

⁵¹⁶ and so for the case where only one photon is detected by the PMT ($k = 1$)

$$P_T(t | \mu_l, \mu_d, k = 1) = I_1 [P(1, \mu_l) P(0, \mu_d) f_l(t) + P(0, \mu_l) P(1, \mu_d) f_d(t)] \quad (2.21)$$

⁵¹⁷ where $P(k_\alpha, \mu_\alpha)$ is the Poisson probability to detect k_α PE from $\alpha \in \{l, d\}$ with the condition $k_l + k_d = k$.

⁵¹⁹ Now that we have the individual timing and charge probability we can construct the charge
⁵²⁰ likelihood referred as QMLE:

$$\mathcal{L}(q_1, q_2, \dots, q_N | \vec{r}, E_{vis}) = \prod_{j \in \text{unfired}} e^{-\mu_j} \prod_{i \in \text{fired}} \left(\sum_{k=1} P_Q(q_i | k) \cdot P(k, \mu_i) \right) \quad (2.22)$$

521 where $\mu_i = E_{vis}\hat{\mu}_i^L + \mu_i^D$ and $P(k, \mu_i)$ is the Poisson probability of observing k PE. $P_Q(q_i|k)$ is the
 522 charge pdf for k PE. And we can also construct the time likelihood referred as TMLE:

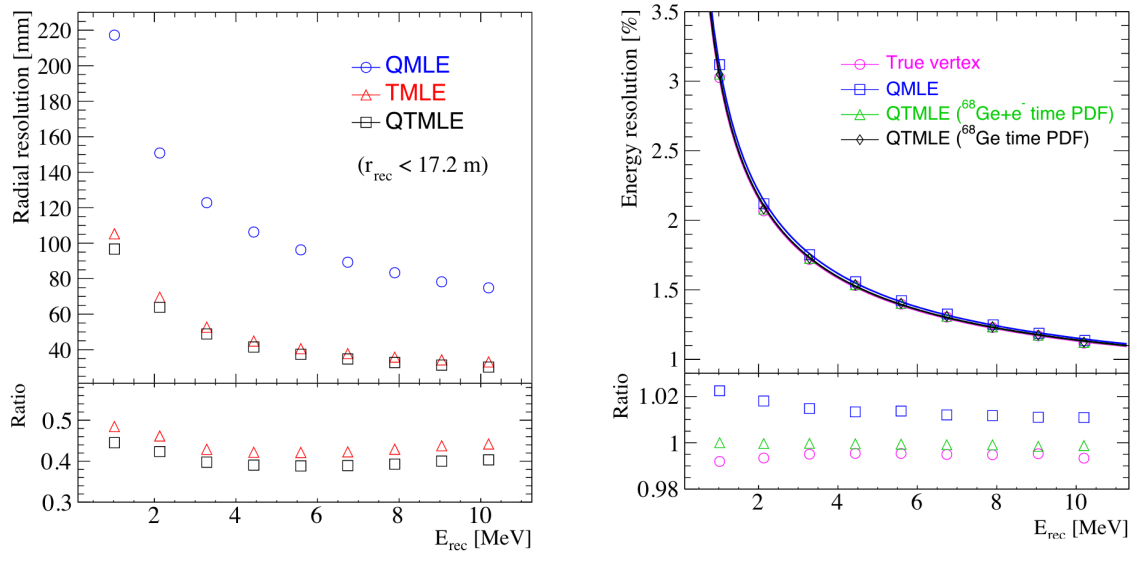
$$\mathcal{L}(t_{1,r}, t_{2,r}, \dots, t_{N,r} | \vec{r}, t_0) = \prod_{i \in \text{hit}} \frac{\sum_{k=1}^K P_T(t_{i,r} | r, d, \mu_i^l, \mu_i^d, k) \cdot P(k, \mu_i^l + \mu_i^d)}{\sum_{k=1}^K P(k, \mu_i^l + \mu_i^d)} \quad (2.23)$$

523 where K is cut to 20 PE and hit is the set of hits satisfying $-100 < t_{i,r} < 500$ ns.

524 Merging those two likelihood give the charge-time likelihood QTMLLE

$$\mathcal{L}(q_1, q_2, \dots, q_N; t_{1,r}, t_{2,r}, \dots, t_{N,r} | \vec{r}, t_0, E_{vis}) = \mathcal{L}(q_1, q_2, \dots, q_N | \vec{r}, E_{vis}) \cdot \mathcal{L}(t_{1,r}, t_{2,r}, \dots, t_{N,r} | \vec{r}, t_0) \quad (2.24)$$

525 The radial and energy resolutions of the different likelihood are presented in figure 2.18 (from
 526 [39]). We can see the improvement of adding the time information to the vertex reconstruction and
 527 that an increase in vertex precision can bring improvement in the energy resolution, especially at low
 528 energies.



(A) Radial resolutions of the likelihood-based algorithm TMLE, QMLE and QTMLLE

(B) Energy resolution of QMLE and QTMLLE using different vertex resolutions

FIGURE 2.18

529 Data driven methods prove to be performant in the energy and vertex reconstruction given that
 530 we have enough calibrations sources to produce the PDF. In the next section, we'll see another type
 531 of data-driven method based on machine learning.

532 2.5.3 Machine learning for reconstruction

533 Machine learning (ML) is family of data-driven algorithms that are inferring behavior and results
 534 from a training dataset. A overview of methods and detailed explanation of the Neural Network
 535 (NN) subfamily can be found in Chapter 3.

536 The power of ML is the ability to model complex response to a specific problem. In JUNO
 537 the reconstruction problematic can be expressed as follow: knowing that each PMT, large or small,
 538 detected a given number of PE Q at a given time t and their position is x, y, z where did the energy

539 was deposited and how much energy was it, modeling a function that naively goes:

$$\mathbb{R}^{5 \times N_{pmt}} \mapsto \mathbb{R}^4 \quad (2.25)$$

540 It is worth pointing that while this is already a lot in informations, this is not the rawest representation
541 of the experiment. We could indeed replace the charge and time by the waveform in the time window of the event but that would lead to an input representation size that would exceed our
542 computational limits. Also, due to those computational limits, most of the ML algorithm reduce this
543 input phase space either by structurally encoding the information (pictures, graph), by aggregating
544 it (mean, variance, ...) or by exploiting invariance and equivariance of the experiment (rotational
545 invariance due to the sphericity, ...).

546 For machine learning to converge to performant algorithm, a large dataset exploring all the phase
547 space of interest is needed. For the following studies, data from the monte carlo simulation presented
548 in section 2.4 are used for training. When the detector will be finished calibrations sources will be
549 complementarily be used.

551 Boosted Decision Tree (BDT)

552 On of the most classic ML method used in physics in last years is the Boosted Decision Tree (see
553 chapter 3.2). They have been explored for vertex reconstruction [40] et for energy reconstruction [40,
554 41].

555 For vertex and energy reconstruction a BDT was developed using the aggregated informations
556 presented in 2.6.

Parameter	description
$nHits$	Total number of hits
$x_{cc}, y_{cc}, z_{cc}, R_{cc}$	Coordinates of the center of charge
ht_{mean}, ht_{std}	Hit time mean and standard deviation

TABLE 2.6 – Features used by the BDT for vertex reconstruction

557 Its reconstruction performances are presented in figure 2.20.

558 A second and more advanced BDT, subsequently named BDTE, that only reconstruct energy use
559 a different set of features [41]. They are presented in the table 2.7

560 Neural Network (NN)

561 The physics have shown a rising for Neural Network (NN) in the past years for event reconstruc-
562 tion, notably in the neutrino community [42–45]. Three type of neural networks have explored for
563 event reconstruction in JUNO Deep Neural Network (DNN), Convolutional Neural Network (CNN)

AccumCharge	$ht_{5\%–2\%}$
R_{cht}	pe_{mean}
z_{cc}	J_{cht}
pe_{std}	ϕ_{cc}
nPMTs	$ht_{35\%–30\%}$
$ht_{kurtosis}$	$ht_{20\%–15\%}$
$ht_{25\%–20\%}$	$pe_{35\%}$
R_{cc}	$ht_{30\%–25\%}$

TABLE 2.7 – Features used by the BDTE algorithm. pe and ht reference the charge and hit-time distribution respectively and the percentages are the quantiles of those distributions. cht and cc reference the barycenters of hit time and charge respectively

and Graph Network (GNN). More explanation about those neural network can be found in chapter 3.

The CNN are using 2D projection of the detector representing it as an image with two channel, one for the charge Q and one for the time t . The position of the PMTs is structurally encoded in the pixel containing the information of this PMT. In [40], the pixel is chosen based on a transformation of θ and ϕ coordinates to the 2D plane and rounded to the nearest pixel. A sufficiently large image has been chosen to prevent two PMT to be located in the same pixel. An example of this projection can be found in figure 2.19. The performances of the CNN can be found in figure 2.20.

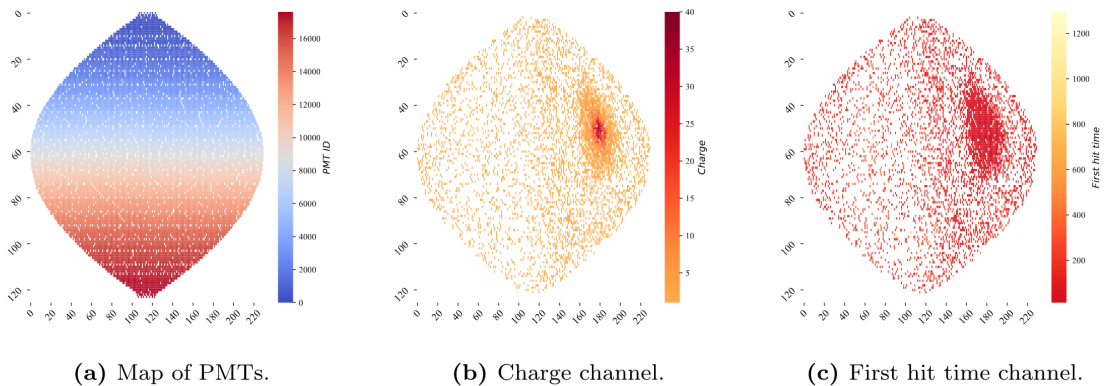


FIGURE 2.19 – Projection of the LPMTs in JUNO on a 2D plane. (a) Show the distribution of all PMTs and (b) and (c) are example of what the charge and time channel looks like respectively

Using 2D have the upside of encoding a large part of the informations structurally but loose the rotational invariance of the detector. It also give undefined information to the neural network (what is a pixel without PMT ? What should be its charge and time ?), cause deformation in the representation of the detector (sides of projection) and loose topological informations.

One of the way to present structurally the sphericity of JUNO to a NN is to use a graph: A collection of objects V called nodes and relations E called edges, each relation associated to a couple v_1, v_2 forming the graph $G(E, V)$. Nodes and edges can hold informations or features. In [40] the nodes, are geometrical region of the detector as defined by the HealPix [46]. The features of the nodes are aggregated informations from the PMTs it contains. The edges contains geographic informations of the nodes relative positions.

This data representation has the advantages to keep the topology of the detector intact. It also permit the use of rotational invariant algorithms for the NN, thus taking advantage of the symmetries of the detector.

The neural network then process the graph using Chebyshev Convolutions [47]. The performances of the GNN are presented in figure 2.20.

Overall ML algorithms show similar performances as classical algorithms in term of energy reconstructions with the more complex structure CNN and GNN showing better performances than BDT and DNN. For vertex reconstruction, the BDT and DNN show poor performance while CNN are on the level of the classical algorithms.

2.6 JUNO sensitivity to NMO and precise measurements

Once the event is reconstructed, and the energy spectrum is produced, we will need to extract the NMO oscillation parameters from it.

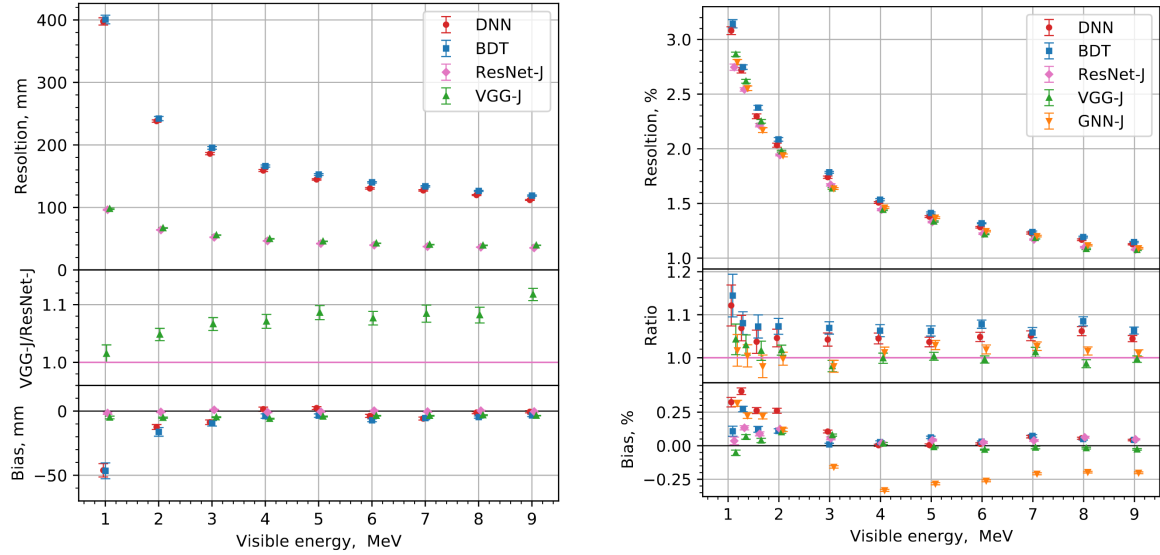


FIGURE 2.20 – Radial (left) and energy (right) resolutions of different ML algorithms. The results presented here are from [40]. DNN is a deep neural network, BDT is a BDT, ResNet-J and VGG-J are CNN and GNN-J is a GNN.

⁵⁹⁴ 2.6.1 Fitting procedure

⁵⁹⁵ **Chapter 3**

⁵⁹⁶ **Machine learning and Artificial
⁵⁹⁷ Neural Network**

⁵⁹⁸ **3.1 History of the Machine learning**

⁵⁹⁹ **3.2 Boosted Decision Tree (BDT)**

⁶⁰⁰ **3.3 Artificial Neural Network (NN)**

⁶⁰¹ **3.3.1 Fully Connected Deep Neural Network (FCDNN)**

⁶⁰² **3.3.2 Convolutional Neural Network (CNN)**

⁶⁰³ **3.3.3 Graph Neural Network (GNN)**

⁶⁰⁴ **3.3.4 Adversarial Neural Network (ANN)**

⁶⁰⁵ **Generative Adversarial Network (GAN)**

⁶⁰⁶ **Reinforcement Learning (RL)**

⁶⁰⁷ **Random Search (RS)**

⁶⁰⁸ **Bayesian Optimization**

⁶⁰⁹ **Chapter 4**

⁶¹⁰ **Image recognition for IBD
reconstruction with the SPMT system**

⁶¹² **Chapter 5**

⁶¹³ **Graph representation of JUNO for IBD
reconstruction with the LPMT system**

⁶¹⁴

⁶¹⁵ Chapter 6

⁶¹⁶ **Reliability of machine learning
methods**

⁶¹⁷

⁶¹⁸ **Chapter 7**

⁶¹⁹ **Discrimination of e+/e- events in
JUNO**

⁶²⁰

621 **Chapter 8**

622 **Conclusion**

Bibliography

- [1] Liang Zhan, Yifang Wang, Jun Cao, and Liangjian Wen. "Determination of the Neutrino Mass Hierarchy at an Intermediate Baseline". *Physical Review D* 78.11 (Dec. 10, 2008), 111103. ISSN: 1550-7998, 1550-2368. DOI: [10 . 1103 / PhysRevD . 78 . 111103](https://doi.org/10.1103/PhysRevD.78.111103). eprint: [0807 . 3203 \[hep-ex, physics:hep-ph\]](https://arxiv.org/abs/0807.3203). URL: [http://arxiv.org/abs/0807.3203](https://arxiv.org/abs/0807.3203) (visited on 09/18/2023).
- [2] Fengpeng An et al. "Neutrino Physics with JUNO". *Journal of Physics G: Nuclear and Particle Physics* 43.3 (Mar. 1, 2016), 030401. ISSN: 0954-3899, 1361-6471. DOI: [10 . 1088 / 0954 - 3899 / 43 / 3 / 030401](https://doi.org/10.1088/0954-3899/43/3/030401). eprint: [1507 . 05613 \[hep-ex, physics:physics\]](https://arxiv.org/abs/1507.05613). URL: [http://arxiv.org/abs/1507.05613](https://arxiv.org/abs/1507.05613) (visited on 07/28/2023).
- [3] Liang Zhan, Yifang Wang, Jun Cao, and Liangjian Wen. "Experimental Requirements to Determine the Neutrino Mass Hierarchy Using Reactor Neutrinos". *Physical Review D* 79.7 (Apr. 14, 2009), 073007. ISSN: 1550-7998, 1550-2368. DOI: [10 . 1103 / PhysRevD . 79 . 073007](https://doi.org/10.1103/PhysRevD.79.073007). eprint: [0901 . 2976 \[hep-ex\]](https://arxiv.org/abs/0901.2976). URL: [http://arxiv.org/abs/0901.2976](https://arxiv.org/abs/0901.2976) (visited on 09/18/2023).
- [4] A. A. Hahn, K. Schreckenbach, W. Gelletly, F. von Feilitzsch, G. Colvin, and B. Krusche. "Antineutrino spectra from 241Pu and 239Pu thermal neutron fission products". *Physics Letters B* 218.3 (Feb. 23, 1989), 365–368. ISSN: 0370-2693. DOI: [10 . 1016 / 0370 - 2693 \(89\) 91598 - 0](https://doi.org/10.1016/0370-2693(89)91598-0). URL: <https://www.sciencedirect.com/science/article/pii/0370269389915980> (visited on 01/16/2024).
- [5] Th A. Mueller et al. "Improved Predictions of Reactor Antineutrino Spectra". *Physical Review C* 83.5 (May 23, 2011), 054615. ISSN: 0556-2813, 1089-490X. DOI: [10 . 1103 / PhysRevC . 83 . 054615](https://doi.org/10.1103/PhysRevC.83.054615). eprint: [1101 . 2663 \[hep-ex, physics:nucl-ex\]](https://arxiv.org/abs/1101.2663). URL: [http://arxiv.org/abs/1101.2663](https://arxiv.org/abs/1101.2663) (visited on 01/16/2024).
- [6] F. von Feilitzsch, A. A. Hahn, and K. Schreckenbach. "Experimental beta-spectra from 239Pu and 235U thermal neutron fission products and their correlated antineutrino spectra". *Physics Letters B* 118.1 (Dec. 2, 1982), 162–166. ISSN: 0370-2693. DOI: [10 . 1016 / 0370 - 2693 \(82\) 90622 - 0](https://doi.org/10.1016/0370-2693(82)90622-0). URL: <https://www.sciencedirect.com/science/article/pii/0370269382906220> (visited on 01/16/2024).
- [7] K. Schreckenbach, G. Colvin, W. Gelletly, and F. Von Feilitzsch. "Determination of the antineutrino spectrum from 235U thermal neutron fission products up to 9.5 MeV". *Physics Letters B* 160.4 (Oct. 10, 1985), 325–330. ISSN: 0370-2693. DOI: [10 . 1016 / 0370 - 2693 \(85\) 91337 - 1](https://doi.org/10.1016/0370-2693(85)91337-1). URL: <https://www.sciencedirect.com/science/article/pii/0370269385913371> (visited on 01/16/2024).
- [8] Patrick Huber. "On the determination of anti-neutrino spectra from nuclear reactors". *Physical Review C* 84.2 (Aug. 29, 2011), 024617. ISSN: 0556-2813, 1089-490X. DOI: [10 . 1103 / PhysRevC . 84 . 024617](https://doi.org/10.1103/PhysRevC.84.024617). eprint: [1106 . 0687 \[hep-ex, physics:hep-ph, physics:nucl-ex, physics:nucl-th\]](https://arxiv.org/abs/1106.0687). URL: [http://arxiv.org/abs/1106.0687](https://arxiv.org/abs/1106.0687) (visited on 01/16/2024).
- [9] P. Vogel, G. K. Schenter, F. M. Mann, and R. E. Schenter. "Reactor antineutrino spectra and their application to antineutrino-induced reactions. II". *Physical Review C* 24.4 (Oct. 1, 1981). Publisher: American Physical Society, 1543–1553. DOI: [10 . 1103 / PhysRevC . 24 . 1543](https://doi.org/10.1103/PhysRevC.24.1543). URL: <https://link.aps.org/doi/10.1103/PhysRevC.24.1543> (visited on 01/16/2024).

- [10] D. A. Dwyer and T. J. Langford. "Spectral Structure of Electron Antineutrinos from Nuclear Reactors". *Physical Review Letters* 114.1 (Jan. 7, 2015), 012502. ISSN: 0031-9007, 1079-7114. DOI: 10.1103/PhysRevLett.114.012502. eprint: 1407.1281[hep-ex, physics:nucl-ex]. URL: <http://arxiv.org/abs/1407.1281> (visited on 01/16/2024).
- [11] JUNO Collaboration et al. "Sub-percent Precision Measurement of Neutrino Oscillation Parameters with JUNO". *Chinese Physics C* 46.12 (Dec. 1, 2022), 123001. ISSN: 1674-1137, 2058-6132. DOI: 10.1088/1674-1137/ac8bc9. eprint: 2204.13249[hep-ex]. URL: <http://arxiv.org/abs/2204.13249> (visited on 08/11/2023).
- [12] JUNO Collaboration et al. *TAO Conceptual Design Report: A Precision Measurement of the Reactor Antineutrino Spectrum with Sub-percent Energy Resolution*. May 18, 2020. DOI: 10.48550/arXiv.2005.08745. eprint: 2005.08745[hep-ex, physics:nucl-ex, physics:physics]. URL: <http://arxiv.org/abs/2005.08745> (visited on 01/18/2024).
- [13] G. Mention, M. Fechner, Th. Lasserre, Th. A. Mueller, D. Lhuillier, M. Cribier, and A. Letourneau. "Reactor antineutrino anomaly". *Physical Review D* 83.7 (Apr. 29, 2011). Publisher: American Physical Society, 073006. DOI: 10.1103/PhysRevD.83.073006. URL: <https://link.aps.org/doi/10.1103/PhysRevD.83.073006> (visited on 03/05/2024).
- [14] V. Kopeikin, M. Skorokhvatov, and O. Titov. "Reevaluating reactor antineutrino spectra with new measurements of the ratio between ^{235}U and ^{239}Pu β^- spectra". *Physical Review D* 104.7 (Oct. 25, 2021), L071301. ISSN: 2470-0010, 2470-0029. DOI: 10.1103/PhysRevD.104.L071301. eprint: 2103.01684[hep-ph, physics:nucl-ex, physics:nucl-th]. URL: <http://arxiv.org/abs/2103.01684> (visited on 01/18/2024).
- [15] A. Letourneau et al. "On the origin of the reactor antineutrino anomalies in light of a new summation model with parameterized β^- transitions". *Physical Review Letters* 130.2 (Jan. 10, 2023), 021801. ISSN: 0031-9007, 1079-7114. DOI: 10.1103/PhysRevLett.130.021801. eprint: 2205.14954[hep-ex, physics:hep-ph]. URL: <http://arxiv.org/abs/2205.14954> (visited on 01/16/2024).
- [16] Particle Data Group et al. "Review of Particle Physics". *Progress of Theoretical and Experimental Physics* 2020.8 (Aug. 14, 2020), 083C01. ISSN: 2050-3911. DOI: 10.1093/ptep/ptaa104. URL: <https://doi.org/10.1093/ptep/ptaa104> (visited on 12/04/2023).
- [17] Super-Kamiokande Collaboration et al. "Diffuse Supernova Neutrino Background Search at Super-Kamiokande". *Physical Review D* 104.12 (Dec. 10, 2021), 122002. ISSN: 2470-0010, 2470-0029. DOI: 10.1103/PhysRevD.104.122002. eprint: 2109.11174[astro-ph, physics:hep-ex]. URL: <http://arxiv.org/abs/2109.11174> (visited on 02/28/2024).
- [18] Alessandro Strumia and Francesco Vissani. "Precise quasielastic neutrino/nucleon cross section". *Physics Letters B* 564.1 (July 2003), 42–54. ISSN: 03702693. DOI: 10.1016/S0370-2693(03)00616-6. eprint: astro-ph/0302055. URL: <http://arxiv.org/abs/astro-ph/0302055> (visited on 01/16/2024).
- [19] Daya Bay et al. *Optimization of the JUNO liquid scintillator composition using a Daya Bay antineutrino detector*. July 1, 2020. DOI: 10.48550/arXiv.2007.00314. eprint: 2007.00314[hep-ex, physics:physics]. URL: <http://arxiv.org/abs/2007.00314> (visited on 07/26/2023).
- [20] J. B. Birks. "CHAPTER 3 - THE SCINTILLATION PROCESS IN ORGANIC MATERIALS—I". *The Theory and Practice of Scintillation Counting*. Ed. by J. B. Birks. International Series of Monographs in Electronics and Instrumentation. Jan. 1, 1964, 39–67. ISBN: 978-0-08-010472-0. DOI: 10.1016/B978-0-08-010472-0.50008-2. URL: <https://www.sciencedirect.com/science/article/pii/B9780080104720500082> (visited on 02/07/2024).
- [21] Photomultiplier tube R12860 | Hamamatsu Photonics. URL: https://www.hamamatsu.com/eu/en/product/optical-sensors/pmt/pmt_tube-alone/head-on-type/R12860.html (visited on 02/08/2024).

- [22] Yan Zhang, Ze-Yuan Yu, Xin-Ying Li, Zi-Yan Deng, and Liang-Jian Wen. "A complete optical model for liquid-scintillator detectors". *Nuclear Instruments and Methods in Physics Research Section A: Accelerators, Spectrometers, Detectors and Associated Equipment* 967 (July 2020), 163860. ISSN: 01689002. DOI: [10.1016/j.nima.2020.163860](https://doi.org/10.1016/j.nima.2020.163860). eprint: [2003.12212\[physics\]](https://arxiv.org/abs/2003.12212). URL: <http://arxiv.org/abs/2003.12212> (visited on 02/07/2024).
- [23] Hai-Bo Yang et al. "Light Attenuation Length of High Quality Linear Alkyl Benzene as Liquid Scintillator Solvent for the JUNO Experiment". *Journal of Instrumentation* 12.11 (Nov. 27, 2017), T11004–T11004. ISSN: 1748-0221. DOI: [10.1088/1748-0221/12/11/T11004](https://doi.org/10.1088/1748-0221/12/11/T11004). eprint: [1703.01867\[hep-ex, physics:physics\]](https://arxiv.org/abs/1703.01867). URL: <http://arxiv.org/abs/1703.01867> (visited on 07/28/2023).
- [24] JUNO Collaboration et al. *The Design and Sensitivity of JUNO's scintillator radiopurity pre-detector OSIRIS*. Mar. 31, 2021. DOI: [10.48550/arXiv.2103.16900](https://doi.org/10.48550/arXiv.2103.16900). eprint: [2103.16900\[physics\]](https://arxiv.org/abs/2103.16900). URL: <http://arxiv.org/abs/2103.16900> (visited on 02/07/2024).
- [25] Angel Abusleme et al. "Mass Testing and Characterization of 20-inch PMTs for JUNO". *The European Physical Journal C* 82.12 (Dec. 24, 2022), 1168. ISSN: 1434-6052. DOI: [10.1140/epjc/s10052-022-11002-8](https://doi.org/10.1140/epjc/s10052-022-11002-8). eprint: [2205.08629\[hep-ex, physics:physics\]](https://arxiv.org/abs/2205.08629). URL: <http://arxiv.org/abs/2205.08629> (visited on 02/08/2024).
- [26] R. Acquafredda et al. "The OPERA experiment in the CERN to Gran Sasso neutrino beam". *Journal of Instrumentation* 4.4 (Apr. 2009), P04018. ISSN: 1748-0221. DOI: [10.1088/1748-0221/4/04/P04018](https://doi.org/10.1088/1748-0221/4/04/P04018). URL: <https://dx.doi.org/10.1088/1748-0221/4/04/P04018> (visited on 02/29/2024).
- [27] Yang Han. "Dual Calorimetry for High Precision Neutrino Oscillation Measurement at JUNO Experiment". AstroParticule et Cosmologie, France, Paris U. VII, APC, June 2021.
- [28] JUNO collaboration et al. "Calibration Strategy of the JUNO Experiment". *Journal of High Energy Physics* 2021.3 (Mar. 2021), 4. ISSN: 1029-8479. DOI: [10.1007/JHEP03\(2021\)004](https://doi.org/10.1007/JHEP03(2021)004). eprint: [2011.06405\[hep-ex, physics:physics\]](https://arxiv.org/abs/2011.06405). URL: <http://arxiv.org/abs/2011.06405> (visited on 08/10/2023).
- [29] Tao Lin et al. "The Application of SNiPER to the JUNO Simulation". *Journal of Physics: Conference Series* 898.4 (Oct. 2017). Publisher: IOP Publishing, 042029. ISSN: 1742-6596. DOI: [10.1088/1742-6596/898/4/042029](https://doi.org/10.1088/1742-6596/898/4/042029). URL: <https://dx.doi.org/10.1088/1742-6596/898/4/042029> (visited on 02/27/2024).
- [30] S. Agostinelli et al. "Geant4—a simulation toolkit". *Nuclear Instruments and Methods in Physics Research Section A: Accelerators, Spectrometers, Detectors and Associated Equipment* 506.3 (July 1, 2003), 250–303. ISSN: 0168-9002. DOI: [10.1016/S0168-9002\(03\)01368-8](https://doi.org/10.1016/S0168-9002(03)01368-8). URL: <https://www.sciencedirect.com/science/article/pii/S0168900203013688> (visited on 02/27/2024).
- [31] J. Allison et al. "Geant4 developments and applications". *IEEE Transactions on Nuclear Science* 53.1 (Feb. 2006). Conference Name: IEEE Transactions on Nuclear Science, 270–278. ISSN: 1558-1578. DOI: [10.1109/TNS.2006.869826](https://doi.org/10.1109/TNS.2006.869826). URL: <https://ieeexplore.ieee.org/document/1610988?isnumber=33833&arnumber=1610988&count=33&index=7> (visited on 02/27/2024).
- [32] J. Allison et al. "Recent developments in Geant4". *Nuclear Instruments and Methods in Physics Research Section A: Accelerators, Spectrometers, Detectors and Associated Equipment* 835 (Nov. 1, 2016), 186–225. ISSN: 0168-9002. DOI: [10.1016/j.nima.2016.06.125](https://doi.org/10.1016/j.nima.2016.06.125). URL: <https://www.sciencedirect.com/science/article/pii/S0168900216306957> (visited on 02/27/2024).
- [33] Wenjie Wu, Miao He, Xiang Zhou, and Haoxue Qiao. "A new method of energy reconstruction for large spherical liquid scintillator detectors". *Journal of Instrumentation* 14.3 (Mar. 8, 2019), P03009–P03009. ISSN: 1748-0221. DOI: [10.1088/1748-0221/14/03/P03009](https://doi.org/10.1088/1748-0221/14/03/P03009). eprint: [1812.01799\[hep-ex, physics:physics\]](https://arxiv.org/abs/1812.01799). URL: <http://arxiv.org/abs/1812.01799> (visited on 07/28/2023).

- [34] Guihong Huang et al. "Improving the energy uniformity for large liquid scintillator detectors". *Nuclear Instruments and Methods in Physics Research Section A: Accelerators, Spectrometers, Detectors and Associated Equipment* 1001 (June 11, 2021), 165287. ISSN: 0168-9002. DOI: [10.1016/j.nima.2021.165287](https://doi.org/10.1016/j.nima.2021.165287). URL: <https://www.sciencedirect.com/science/article/pii/S0168900221002710> (visited on 03/01/2024).
- [35] Ziyuan Li et al. "Event vertex and time reconstruction in large volume liquid scintillator detector". *Nuclear Science and Techniques* 32.5 (May 2021), 49. ISSN: 1001-8042, 2210-3147. DOI: [10.1007/s41365-021-00885-z](https://doi.org/10.1007/s41365-021-00885-z). eprint: [2101.08901\[hep-ex, physics:physics\]](https://arxiv.org/abs/2101.08901). URL: [http://arxiv.org/abs/2101.08901](https://arxiv.org/abs/2101.08901) (visited on 07/28/2023).
- [36] Gioacchino Ranucci. "An analytical approach to the evaluation of the pulse shape discrimination properties of scintillators". *Nuclear Instruments and Methods in Physics Research Section A: Accelerators, Spectrometers, Detectors and Associated Equipment* 354.2 (Jan. 30, 1995), 389–399. ISSN: 0168-9002. DOI: [10.1016/0168-9002\(94\)00886-8](https://doi.org/10.1016/0168-9002(94)00886-8). URL: <https://www.sciencedirect.com/science/article/pii/0168900294008868> (visited on 03/07/2024).
- [37] C. Galbiati and K. McCarty. "Time and space reconstruction in optical, non-imaging, scintillator-based particle detectors". *Nuclear Instruments and Methods in Physics Research Section A: Accelerators, Spectrometers, Detectors and Associated Equipment* 568.2 (Dec. 1, 2006), 700–709. ISSN: 0168-9002. DOI: [10.1016/j.nima.2006.07.058](https://doi.org/10.1016/j.nima.2006.07.058). URL: <https://www.sciencedirect.com/science/article/pii/S0168900206013519> (visited on 03/07/2024).
- [38] M. Moszyński and B. Bengtson. "Status of timing with plastic scintillation detectors". *Nuclear Instruments and Methods* 158 (Jan. 1, 1979), 1–31. ISSN: 0029-554X. DOI: [10.1016/S0029-554X\(79\)90170-8](https://doi.org/10.1016/S0029-554X(79)90170-8). URL: <https://www.sciencedirect.com/science/article/pii/S0029554X79901708> (visited on 03/07/2024).
- [39] Gui-Hong Huang, Wei Jiang, Liang-Jian Wen, Yi-Fang Wang, and Wu-Ming Luo. "Data-driven simultaneous vertex and energy reconstruction for large liquid scintillator detectors". *Nuclear Science and Techniques* 34.6 (June 17, 2023), 83. ISSN: 2210-3147. DOI: [10.1007/s41365-023-01240-0](https://doi.org/10.1007/s41365-023-01240-0). URL: <https://doi.org/10.1007/s41365-023-01240-0> (visited on 08/17/2023).
- [40] Zhen Qian et al. "Vertex and Energy Reconstruction in JUNO with Machine Learning Methods". *Nuclear Instruments and Methods in Physics Research Section A: Accelerators, Spectrometers, Detectors and Associated Equipment* 1010 (Sept. 2021), 165527. ISSN: 01689002. DOI: [10.1016/j.nima.2021.165527](https://doi.org/10.1016/j.nima.2021.165527). eprint: [2101.04839\[hep-ex, physics:physics\]](https://arxiv.org/abs/2101.04839). URL: [http://arxiv.org/abs/2101.04839](https://arxiv.org/abs/2101.04839) (visited on 07/24/2023).
- [41] Arsenii Gavrikov, Yury Malyshkin, and Fedor Ratnikov. "Energy reconstruction for large liquid scintillator detectors with machine learning techniques: aggregated features approach". *The European Physical Journal C* 82.11 (Nov. 14, 2022), 1021. ISSN: 1434-6052. DOI: [10.1140/epjc/s10052-022-11004-6](https://doi.org/10.1140/epjc/s10052-022-11004-6). eprint: [2206.09040\[physics\]](https://arxiv.org/abs/2206.09040). URL: [http://arxiv.org/abs/2206.09040](https://arxiv.org/abs/2206.09040) (visited on 07/24/2023).
- [42] R. Abbasi et al. "Graph Neural Networks for low-energy event classification & reconstruction in IceCube". *Journal of Instrumentation* 17.11 (Nov. 2022). Publisher: IOP Publishing, P11003. ISSN: 1748-0221. DOI: [10.1088/1748-0221/17/11/P11003](https://doi.org/10.1088/1748-0221/17/11/P11003). URL: <https://dx.doi.org/10.1088/1748-0221/17/11/P11003> (visited on 04/04/2024).
- [43] S. Reck, D. Guderian, G. Vermarien, A. Domi, and on behalf of the KM3NeT collaboration on behalf of the. "Graph neural networks for reconstruction and classification in KM3NeT". *Journal of Instrumentation* 16.10 (Oct. 2021). Publisher: IOP Publishing, C10011. ISSN: 1748-0221. DOI: [10.1088/1748-0221/16/10/C10011](https://doi.org/10.1088/1748-0221/16/10/C10011). URL: <https://dx.doi.org/10.1088/1748-0221/16/10/C10011> (visited on 04/04/2024).
- [44] The IceCube collaboration et al. "A convolutional neural network based cascade reconstruction for the IceCube Neutrino Observatory". *Journal of Instrumentation* 16.7 (July 2021). Publisher: IOP Publishing, P07041. ISSN: 1748-0221. DOI: [10.1088/1748-0221/16/07/P07041](https://doi.org/10.1088/1748-0221/16/07/P07041). URL: <https://dx.doi.org/10.1088/1748-0221/16/07/P07041> (visited on 04/04/2024).

- 809 [45] DUNE Collaboration et al. “Neutrino interaction classification with a convolutional neural
810 network in the DUNE far detector”. *Physical Review D* 102.9 (Nov. 9, 2020). Publisher: American
811 Physical Society, 092003. DOI: [10.1103/PhysRevD.102.092003](https://doi.org/10.1103/PhysRevD.102.092003). URL: <https://link.aps.org/doi/10.1103/PhysRevD.102.092003> (visited on 04/04/2024).
- 813 [46] K. M. Górski, E. Hivon, A. J. Banday, B. D. Wandelt, F. K. Hansen, M. Reinecke, and M. Bartel-
814 mann. “HEALPix: A Framework for High-Resolution Discretization and Fast Analysis of Data
815 Distributed on the Sphere”. *The Astrophysical Journal* 622 (Apr. 1, 2005). ADS Bibcode: 2005ApJ...622..759G,
816 759–771. ISSN: 0004-637X. DOI: [10.1086/427976](https://doi.org/10.1086/427976). URL: <https://ui.adsabs.harvard.edu/abs/2005ApJ...622..759G> (visited on 04/04/2024).
- 818 [47] Michaël Defferrard, Xavier Bresson, and Pierre Vandergheynst. *Convolutional Neural Networks
819 on Graphs with Fast Localized Spectral Filtering*. Feb. 5, 2017. DOI: [10.48550/arXiv.1606.09375](https://doi.org/10.48550/arXiv.1606.09375).
820 eprint: [1606.09375\[cs, stat\]](https://arxiv.org/abs/1606.09375). URL: <http://arxiv.org/abs/1606.09375> (visited on
821 04/04/2024).